J. Fluid Mech. (1987), *vol.* 181, *pp.* 99–140
Printed in Great Britain

The impact of a vortex ring on a wall

By J. D. A. WALKER, C. R. SMITH,
Department of Mechanical Engineering and Mechanics, Lehigh University, Bethlehem, PA, USA

A. W. CERRA
Steam Turbine Division, General Electric Corp., Boston, MA, USA

AND T. L. DOLIGALSKI
US Army Research Office, Research Triangle Park, NC, USA

(Received 17 December 1986)

The flow induced by a vortex ring approaching a plane wall on a trajectory normal to the wall is investigated for an incompressible fluid which is otherwise stagnant. The detailed characteristics of the interaction of the ring with the flow near the surface have been observed experimentally for a wide variety of laminar rings, using dye in water to visualize the flow in the ring as well as near the plane surface. Numerical solutions are obtained for the trajectory of the ring as well as for the unsteady boundary-layer flow that develops on the wall. The experimental and theoretical results show that an unsteady separation develops in the boundary-layer flow, in the form of a secondary ring attached to the wall. A period of explosive boundary-layer growth then ensues and a strong viscous–inviscid interaction occurs in the form of the ejection of the secondary vortex ring from the boundary layer. The primary ring then interacts with the secondary ring and in some cases was observed to induce the formation of a third, tertiary, ring near the wall. The details of this process are investigated over a wide Reynolds number range. The results clearly show how one vortex ring can produce another, through an unsteady interaction with a viscous flow near the wall.

1. Introduction

Over the past fifteen years, there has been an increasing amount of research in flows associated with vortex motions. As experimental flow visualization methods and quantitative measurement techniques have improved, it has become increasingly apparent that vortex motions play an important role in the flow dynamics of such diverse situations as turbulent boundary-layer and turbulent wake flows, mixing layers, airfoils and the wakes of aircraft and turbine blades. The study of vortex motion is rather broad, and in recent times a variety of aspects have been reviewed by Saffman & Baker (1979) and Leonard (1980, 1985). The present study is concerned with the nature of the flow near a solid wall which is induced by vortex motion, and consequently attention will be restricted here to such flows.

In recent years, the recognition that vortex motions are an important feature in the dynamics of the turbulent boundary layer has led to an increasing interest in developing an understanding of the types of flow induced by a moving vortex (see, for example, Acarlar & Smith 1984, 1987*a*, *b*; Doligalski & Walker 1984). One

dominant physical process in turbulent boundary layers is the bursting phenomenon; in this event, violent and abrupt eruptions of fluid from the region near the wall are observed to occur intermittently at isolated spanwise and streamwise locations. It is in this way that new vorticity is continually introduced into the outer layer of the turbulent boundary layer from the near-wall region. Since this is the fundamental manner in which a turbulent boundary layer sustains itself, it is clearly of interest to understand the physical mechanisms which drive this regenerative process. In an early experimental study by Nychas, Hershey & Brodkey (1973), it was suggested that bursting near the wall was somehow associated with the passage of what appeared to be a transverse vortex in the outer region of the boundary layer. Since that time, a number of investigators have sought to isolate the effects of a moving vortex in rather controlled situations.

One of the first experimental investigations which showed that a moving vortex could induce eruptions from a boundary-layer flow near a wall, is due to Harvey & Perry (1971); their study was carried out to determine why aircraft trailing vortices were invariably observed to rebound from a ground plane, in apparent contradiction to the predictions of inviscid theory. A wing was mounted in the sidewall of a wind tunnel that had a moving floor in the test section in order to simulate the effects of an aircraft near the ground . A series of total head surveys indicated that the vortex trailing from the wingtip caused a boundary-layer separation in the form of a secondary eddy which was initially attached to the tunnel floor. At successive stations downstream, an ejection of the secondary eddy from the boundary layer was observed; the viscous–inviscid interaction was so strong that the motion of the trailing vortex was arrested and a rebound occurred from the tunnel floor. The interpretations of Harvey & Perry (1971) were subsequently supported by Walker (1978) who computed the boundary-layer flow induced by a vortex of positive rotation above a plane wall in an otherwise stagnant fluid. Inviscid theory predicts that such a vortex will move at constant speed on a trajectory parallel to the wall. However, a region of adverse pressure gradient is induced on the boundary-layer flow near the wall in front of the moving vortex; separation occurs soon after the initiation of the motion, in the form of a secondary eddy which is of opposite rotation to the primary vortex. The numerical solutions ultimately exhibited strong and apparently explosive boundary-layer growth near the secondary eddy and suggest that the boundary-layer solution was rapidly evolving toward a strong viscous–inviscid interaction with the outer flow. Rational methods to compute such strong interactions are not yet available but the results of Walker (1978) and Harvey & Perry (1971) confirm that the outcome of the process is a boundary-layer eruption and the ejection of a secondary vortex.

In subsequent studies, Doligalski, Smith & Walker (1980) and Doligalski & Walker (1984) have investigated the boundary layer due to a vortex of negative rotation which is convected to the right in a shear flow and a uniform flow respectively. In such situations, a region of adverse pressure gradient occurs behind the moving vortex near the wall. Numerical solutions for the boundary-layer development near the wall showed that separation usually occurred in the form of a detached secondary eddy; in all cases the onset of explosive boundary-layer growth was ultimately observed. Similar behaviour has been observed by Ersoy & Walker (1985*a*, *b*) who studied the boundary-layer effects due to a rectilinear vortex pair near a wall. In all of these studies, a variety of complex and unusual separation effects are produced in the boundary-layer flow by the moving vortices. However, the one common thread

is the following: once a two-dimensional vortex is close enough to a wall for a sufficient period of time, boundary-layer separation and explosive boundary-layer growth are apparently inevitable. This boundary-layer growth is expected to lead to strong viscous–inviscid interaction in the form of a boundary-layer eruption and the evolution of secondary vortices.

One aspect which is normally considered important in the time-dependent motion in a turbulent boundary layer is vortex stretching; however, the previously cited theoretical studies of vortex-induced boundary-layer flows lack this feature, since they are purely two-dimensional flows. Perhaps the most fundamental flow which incorporates vortex stretching is that due to a vortex ring approaching a plane wall in an otherwise stagnant fluid, and this flow is the subject of the present study. When the trajectory of a vortex ring is initially normal to the wall, the inviscid problem can be considered to consist of two vortex rings of opposite circulation approaching one another along a common axis. This mathematical problem was originally considered by Helmholtz (1867) (see also Lamb 1932) who showed that ideal-fluid theory predicts that as a ring approaches the wall, its rate of approach slows and the ring diameter continually increases. As the ring diameter expands, the vortex stretches and the cross-sectional area of the vortex core decreases.

The predictions of ideal-fluid theory are not fully realized in the laboratory. Over the years, there has been a variety of flow visualization studies of the effects of a vortex ring moving in a direction normal to a solid surface (Magarvey & MacLatchey 1964; Boldes & Ferreri 1973; Schneider 1978*a*, *b*; Yamada & Matsui 1980). These studies have been critically reviewed by Cerra & Smith (1983). By and large, all authors found that once the vortex ring approached the wall, there was a significant departure from the trajectory predicted by inviscid theory in the sense that the ring was always observed to rebound from the wall. In most cases, a second vortex ring was observed to form in the boundary layer on the wall, with the secondary ring having a circulation of the opposite sense to that of the primary ring. The secondary ring was observed to be subsequently ejected from the boundary layer and then to interact with the original ring.

In the present paper, the results of a combined theoretical and experimental study of the effects of a vortex ring impacting a solid surface will be described. In §2, the inviscid solution for a ring approaching a wall is described; the formulation of the boundary-layer problem near the wall is described in §3. The actual solutions computed are tied to the experimental cases considered; the experimental apparatus is described in §4 and the detailed flow-visualization results are discussed in §5. Numerical results for the ring trajectories are compared with experiment in §6. The numerical method for the computation of the boundary-layer flow is described in §7 and calculated results are discussed and compared with experiment in §8. A discussion of results follows in §9.

2. The inviscid flow

Consider the inviscid flow produced by a circular vortex ring which approaches a plane impermeable wall in an otherwise unbounded incompressible flow. If all locations on the centre of the ring core are initially equidistant from the wall, the flow is axisymmetric about a normal through the plane of the ring and will remain so for all time t^*. The important geometrical details of the ring are sketched in figure 1. The major radius of the ring $R^*(t^*)$ and the core radius $a^*(t)$ are functions of time,

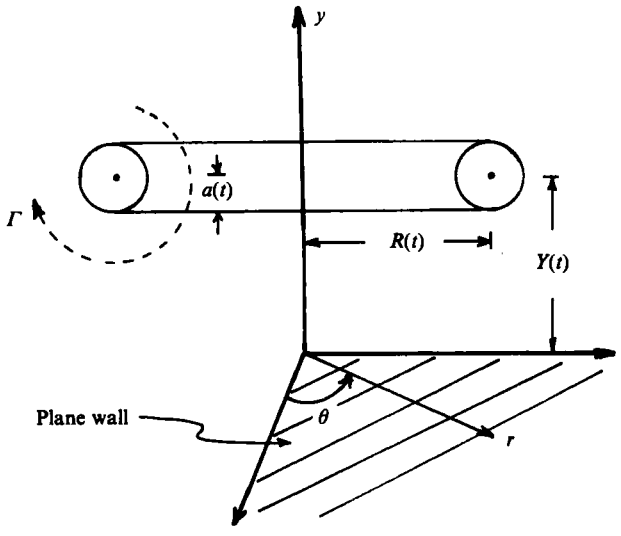

FIGURE 1. Schematic sketch of the geometry for a circular vortex ring approaching a plane wall.

and change as the ring moves toward the wall; at any stage, all points at the centre of the ring core are located a distance $Y^*(t^*)$ from the plane wall. In addition the ring is taken to have a constant circulation Γ, as shown in figure 1. To describe the problem mathematically, cylindrical coordinates (r^*, θ, y^*) are adopted, with origin in the flat plate and on the symmetry axis of the ring; the corresponding velocity components are $(u_r^*, 0, u_y^*)$, since the azimuthal velocity component is taken to be zero. At $t^* = 0$, it is assumed that the ring is located at $r^* = R_0^*$ and $y^* = Y_0^*$. It is evident that both R_0^* and Y_0^* are important in the description of this problem and a representative length L may be defined according to

$$L = (R_0^{*2} + Y_0^{*2})^{\frac{1}{2}}, \tag{1}$$

corresponding to the initial distance of the centre of the core from the origin. A set of dimensionless variables (without the asterisk) may be defined using L and Γ/L as the representative length and velocity respectively, and it is convenient to introduce an axisymmetric streamfunction $\psi(r, y, t)$ defined by

$$u_r = \frac{1}{r}\frac{\partial \psi}{\partial y}, \quad u_y = -\frac{1}{r}\frac{\partial \psi}{\partial r}. \tag{2}$$

The streamfunction corresponding to a circular ring of infinitesimal cross-section $(a/R \to 0)$ in an unbounded fluid was first given by Helmholtz (1867); the inviscid flow due to a vortex ring approaching a wall is readily constructed from this solution and is

$$\psi(r, y, t) = \frac{(Rr)^{\frac{1}{2}}}{2\pi k}\{(2-k^2)\,K(k) - 2E(K)\} - \frac{(Rr)^{\frac{1}{2}}}{2\pi \bar{k}}\{(2-\bar{k}^2)\,K(\bar{k}) - 2E(\bar{k})\}, \tag{3}$$

where

$$k^2 = \frac{4Rr}{(y-Y)^2 + (r+R)^2}, \quad \bar{k}^2 = \frac{4rR}{(y+Y)^2 + (r+R)^2}, \tag{4}$$

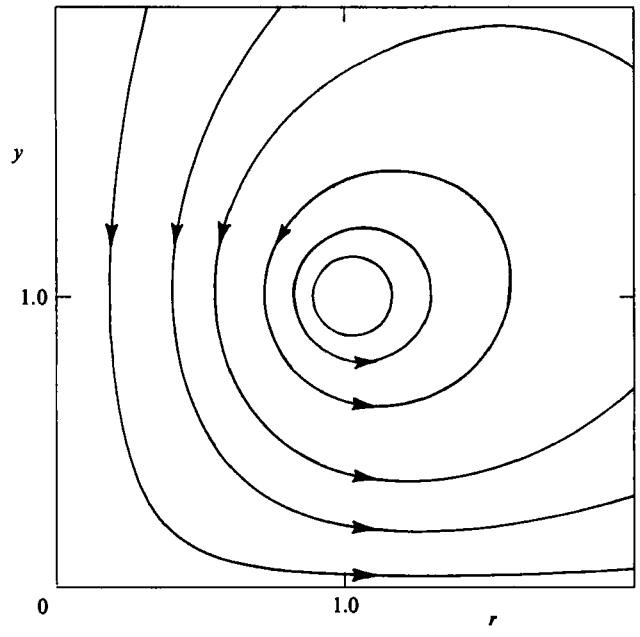

FIGURE 2. Instantaneous inviscid streamlines for a vortex ring above a plane ($Y = R = 1$).

and K and E are complete elliptic integrals of the first and second kinds defined by†

$$K(k) = \int_0^{\frac{1}{2}\pi} (1-k^2 \sin^2 x)^{-\frac{1}{2}}\,\mathrm{d}x, \quad E(k) = \int_0^{\frac{1}{2}\pi} (1-k^2 \sin^2 x)^{\frac{1}{2}}\,\mathrm{d}x. \tag{5}$$

The streamfunction given by (3) describes the instantaneous inviscid flow due to a ring of radius R located a distance Y above the wall, and the instantaneous streamlines for a typical case ($Y = 1.0$, $R = 1.0$) are illustrated in figure 2.

An isolated vortex ring in an unbounded fluid moves parallel to its own axis with nearly constant velocity. For the situation of interest in this paper, the primary vortex ring approaches its image in the wall; it is evident that the velocity field induced by the image will act to slow the rate of approach to the wall and also to increase the radius of the primary ring. Consequently the lengths R and Y are functions of time to be determined. The velocity field of the primary ring consists of a self-induced component and a component induced by the image vortex, which will be denoted by subscripts s and i respectively. The velocity field induced by the image is readily obtained by considering the streamfunction due to the image, applying equations (2) and formally setting $r = R, y = Y$ to obtain the image-induced field at the primary ring according to

$$u_{ri} = \frac{\bar{k}}{4\pi Y}\{2B(\bar{k}) - E(\bar{k})\}, \quad u_{yi} = \frac{\bar{k}^3}{4\pi R} D(\bar{k}). \tag{6}$$

† There is some ambiguity in the definition of elliptic integrals in the literature, and throughout this paper, notation corresponding to Jahnke & Emde (1945) is used.

Here $B(k)$ and $D(k)$ are related to the complete elliptic integrals, and are defined by Jahnke & Emde (1945) according to

$$B(k) = \frac{E(k) - k'^2 K(k)}{k^2}, \quad D(k) = \frac{K(k) - E(k)}{k^2}. \tag{7}$$

In these equations, k' is defined by

$$k'^2 = 1 - k^2, \tag{8}$$

and in (6), $\bar{k}$ is evaluated at $r = R$, $y = Y$.

The self-induced velocity of the vortex ring is not unique in general. A curved line vortex of infinitesimal cross-section will move locally with infinite speed; it is therefore necessary to take into account the effect of a finite-size (but small) core radius and to consider effects of the internal core structure in evaluating the self-induced velocity of the ring. The inviscid solution (3) is an outer solution which is valid at locations remote from the vortex core and which must be matched to an inner solution describing the distribution of vorticity within the core (Tung & Ting 1967; Bliss 1970; Widnall, Bliss & Zalay 1971). For circular vortex rings with a uniform distribution of vorticity across a circular core, the self-induced velocity was first given by Thomson in an appendix to a paper by Helmholtz (1867); this solution gives

$$u_{rs} = 0, \quad u_{ys} = -\frac{1}{4\pi R}\left\{\log\left(\frac{8R}{a}\right) - \frac{1}{4}\right\}, \tag{9a, b}$$

which is valid for $a/R \ll 1$. The speed of propagation given in (9) may be interpreted as the leading term in an expansion in the parameter a/R. The next term in the expansion has been given by Fraenkel (1972) and is $O(a^2/R^2)$; for the vortex rings considered in this study, the second-order term may reasonably be neglected. Perhaps the simplest type of vortex ring corresponds to the physical situation where the fluid in the vortex core is in a state of solid-body rotation and this type of vortex is known as a Kelvin–Hicks ring. Fraenkel (1972) has examined the conditions under which other core models for the ring vortex may exist. Examples of other types of core models have been discussed by Hicks (1884), Saffman (1970) and Bliss (1970). In principle, any distribution of swirl and axial velocity is possible within the vortex core subject to the restrictions

$$\bar{v} = 0 \text{ at } \frac{r}{a} = 0, \quad \bar{v} = O\left(\frac{a}{r}\right) \quad \text{as } \frac{r}{a} \to \infty. \tag{10}$$

Here (r/a) measures dimensionless radial distance from the centre of the vortex core and $\bar{v}$ denotes the swirl velocity about the core. In (10) the last condition is necessary to match to the outer inviscid solution. Evidently a variety of swirl velocity distributions may be selected and the apparent indeterminacy is due to a lack of knowledge of the conditions present when the ring was created. The propagation velocity of the ring depends on integrals of the assumed distributions of swirl and axial velocity in the vortex core; however, the dependence is relatively weak and essentially only affects the constant term on the right-hand side of (9*b*). The Kelvin–Hicks ring appears to be a suitable model for the observed behaviour of the vortex rings observed experimentally in this study and consequently was used exclusively in the theoretical analysis.

It is well known that a vortex line always consists of the same fluid particles and

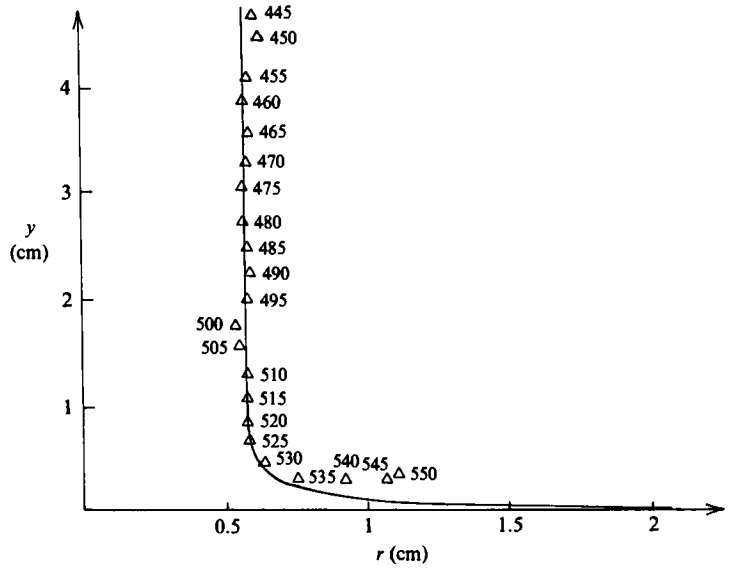

FIGURE 3. Comparison of computed vortex ring trajectory with data.

therefore moves with the fluid in an incompressible flow (see, for example, Milne-Thomson 1962 p. 84). Consequently the core of the Kelvin–Hicks ring under consideration must be of constant volume and it follows that

$$R(t)\,a^2(t) = C, \tag{11}$$

where C is a constant related to the initial volume of the core of the ring. Upon substitution in (9), it follows that

$$u_{ys} = -\frac{1}{8\pi R}\left[\log\left(\frac{64R^3}{C}\right) - \frac{1}{2}\right]. \tag{12}$$

The ring trajectory for a given initial major radius R_0 and height from the wall Y_0 may be obtained by solving the system

$$\frac{\mathrm{d}R}{\mathrm{d}t} = u_{r1}, \quad \frac{\mathrm{d}Y}{\mathrm{d}t} = u_{y1} + u_{ys}, \quad R(0) = R_0, \quad Y(0) = Y_0. \tag{13}$$

These equations were solved numerically using a fourth-order Runge–Kutta integration scheme performed with various sequences of increasingly small timesteps in order to ensure good accuracy. A typical trajectory is given in figure 3 which also includes data points from a trajectory of the present experiments; discussion of the data on this figure is deferred until §5.

Once a numerical solution for the ring trajectory has been produced for given initial conditions, $R(t)$ and $Y(t)$ are known and the time-dependent inviscid velocity distribution induced by the moving ring near the wall may be evaluated. In particular, using (2) and (3), the vertical and radial velocity components may be evaluated and formally letting $y \to 0$ yields

$$u_r \to U_\infty(r, t), \quad u_y \to 0, \tag{14}$$

where

$$U_\infty(r,t) = \frac{Yk_0^3\{2B(k_0)-E(k_0)\}}{4\pi R^{\frac{1}{2}}r^{\frac{3}{2}}(1-k_0^2)}, \quad k_0^2 = \frac{4rR}{Y^2+(r+R)^2}. \tag{15}$$

Evidently the inviscid solution is not uniformly valid. The radial component of velocity is reduced to relative rest on the wall by an unsteady viscous boundary layer which is considered next.

3. Boundary-layer formulation

To describe the boundary-layer flow near the wall, the following scaled variables are defined:

$$u = u_r, \quad v = u_y\, Re^{\frac{1}{2}}, \quad y' = y\, Re^{\frac{1}{2}}, \tag{16}$$

where the Reynolds number for the flow is defined according to $Re = \Gamma/\nu$, with ν the kinematic viscosity. The equations governing the incompressible boundary-layer flow are

$$\frac{1}{r}\frac{\partial}{\partial r}(ru)+\frac{\partial v}{\partial y'} = 0, \tag{17}$$

$$\frac{\partial u}{\partial t}+u\frac{\partial u}{\partial r}+v\frac{\partial u}{\partial y'} = \frac{\partial U_\infty}{\partial t}+U_\infty\frac{\partial U_\infty}{\partial r}+\frac{\partial^2 u}{\partial y'^2}, \tag{18}$$

where t measures dimensionless time from the initial vortex configuration and U_∞ is the dimensionless inviscid radial velocity given by (15). The boundary conditions associated with (17) and (18) are

$$u = v = 0 \quad \text{at } y = 0, \quad u \to U_\infty(r,t) \quad \text{as } y \to \infty. \tag{19}$$

In regard to the initial condition, it is assumed that at $t = 0$ the vortex ring is inserted abruptly into an otherwise stagnant fluid above the infinite plane wall at $r = R_0$, $y = Y_0$. This initial condition is an approximate representation of the experiments, which will subsequently be discussed, in which a vortex ring was abruptly created in the fluid. Upon introduction of the vortex ring, a thin viscous boundary layer begins to form on the wall; to describe the development of this layer mathematically it is convenient to introduce Rayleigh variables according to

$$\eta = \frac{y'}{2t^{\frac{1}{2}}}, \quad \psi = 2t^{\frac{1}{2}}Re^{-\frac{1}{2}}rU_\infty F(r,\eta,t), \tag{20}$$

where ψ is the streamfunction defined by (2). It is easily shown that (18) becomes

$$\frac{\partial^3 F}{\partial\eta^3}+2\eta\frac{\partial^2 F}{\partial\eta^2}-4t\frac{\partial^2 F}{\partial\eta\,\partial t} = 4t\left[\frac{\partial U_\infty}{\partial r}\left[\left(\frac{\partial F}{\partial\eta}\right)^2-1\right]+U_\infty\frac{\partial F}{\partial\eta}\frac{\partial^2 F}{\partial\eta\,\partial r}\right.$$
$$\left.-\left(\frac{U_\infty F}{r}+F\frac{\partial U_\infty}{\partial r}+U_\infty\frac{\partial F}{\partial r}\right)\frac{\partial^2 F}{\partial\eta^2}+\frac{1}{U_\infty}\frac{\partial U_\infty}{\partial t}\left(\frac{\partial F}{\partial\eta}-1\right)\right]. \tag{21}$$

The boundary conditions associated with (21) are

$$F = \frac{\partial F}{\partial\eta} = 0 \quad \text{at } \eta = 0, \quad \frac{\partial F}{\partial\eta} \to 1 \quad \text{as } \eta \to \infty. \tag{22}$$

The initial condition for F may be obtained by letting t approach zero in (21) to obtain

$$\frac{\partial^3 F}{\partial\eta^3}+2\eta\frac{\partial^2 F}{\partial\eta^2} = 0, \tag{23}$$

and the solution of (23) which satisfies conditions (22) is

$$\frac{\partial F}{\partial \eta} = \operatorname{erf}\eta, \quad F = \eta \operatorname{erf}\eta + \frac{1}{\pi^{\frac{1}{2}}} e^{-\eta^2} - \frac{1}{\pi^{\frac{1}{2}}}. \tag{24}$$

These equations provide the initial condition for the boundary-layer flow from which the solution of (21) develops forward in time. However, the formulation of the mathematical problem is not yet complete, since the solution at $r = 0$ and at upstream infinity develops independently of the solution for $0 < r < \infty$; it is therefore necessary to address each of these problems separately and this aspect is considered next.

First consider the solution near $r = 0$. As $r \to 0$, $k_0 \to 0$, and in this limit the elliptic integrals in (15) may be expanded to show that

$$U_\infty \to \alpha(t)\, r + \ldots, \quad \alpha(t) = \frac{3YR^2}{2(Y^2+R^2)^{\frac{5}{2}}}. \tag{25}$$

Substitution of (25) into (21) and taking the limit as $r \to 0$ results in

$$\frac{\partial^3 F_0}{\partial \eta^3} + 2\eta \frac{\partial^2 F_0}{\partial \eta^2} - 4t \frac{\partial^2 F_0}{\partial \eta\, \partial t} = 4\alpha t \left[\left(\frac{\partial F_0}{\partial \eta} \right)^2 - 1 - 2F_0 \frac{\partial^2 F_0}{\partial \eta^2} \right] + \frac{4t}{\alpha} \frac{\mathrm{d}\alpha}{\mathrm{d}t} \left[\frac{\partial F_0}{\partial \eta} - 1 \right]. \tag{26}$$

Here $F_0(\eta, t)$ is defined by

$$F_0(\eta, t) = \lim_{r \to 0} F(r, \eta, t). \tag{27}$$

The function F_0 satisfies the boundary conditions (22) and has the same initial condition given by (24). In (26),

$$\frac{\mathrm{d}\alpha}{\mathrm{d}t} = \frac{3R}{2(Y^2+R^2)^{\frac{7}{2}}} \left[(R^3 - 4Y^2R) \frac{\mathrm{d}Y}{\mathrm{d}t} + (2Y^3 - 3YR^2) \frac{\mathrm{d}R}{\mathrm{d}t} \right], \tag{28}$$

and $\mathrm{d}Y/\mathrm{d}t$ and $\mathrm{d}R/\mathrm{d}t$ are given by (13). The solution of (26) describes an unsteady-stagnation-point flow which develops independently of the rest of the boundary-layer solution. Equation (26) is a nonlinear equation for $F_0(\eta, t)$ and was solved numerically; discussion of the numerical solution is deferred until §7.

Now consider the limit as $r \to \infty$ for which $k_0^2 \sim 4R/r$. It may readily be shown that the inviscid radial velocity given by (15) behaves according to

$$U_\infty(r, t) \sim \frac{\beta(t)}{r^4} + \ldots, \quad \beta(t) = \tfrac{3}{2} YR^2. \tag{29}$$

If the limit $r \to \infty$ is formally taken in (21), it follows that the streamfunction satisfies

$$\frac{\partial^3 F_1}{\partial \eta^3} + 2\eta \frac{\partial^2 F_1}{\partial \eta^2} - 4t \frac{\partial^2 F_1}{\partial \eta\, \partial t} = \frac{4t}{\beta(t)} \frac{\mathrm{d}\beta}{\mathrm{d}t} \left(\frac{\partial F_1}{\partial \eta} - 1 \right), \tag{30}$$

where $F_1(\eta, t)$ is defined by

$$F_1(\eta, t) = \lim_{r \to \infty} F(r, \eta, t). \tag{31}$$

Again the function F_1 satisfies the boundary conditions (22) and has the same initial condition as given by (24). In (30)

$$\frac{\mathrm{d}\beta}{\mathrm{d}t} = \frac{3}{2} \left(R^2 \frac{\mathrm{d}Y}{\mathrm{d}t} + 2RY \frac{\mathrm{d}R}{\mathrm{d}t} \right), \tag{32}$$

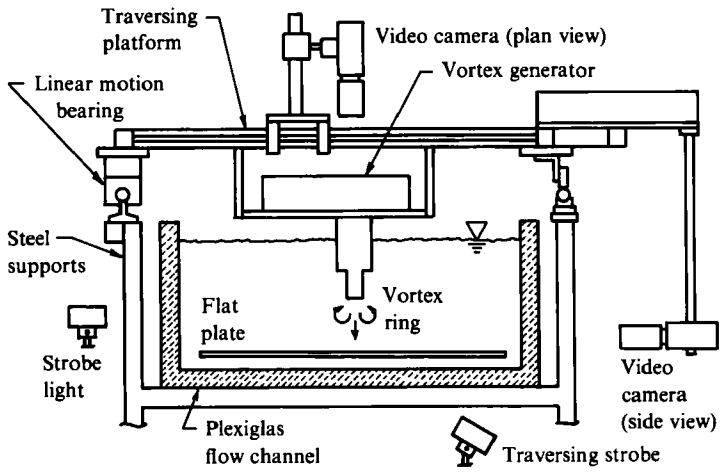

FIGURE 4. End-on view of water channel and traversing platform.

where dY/dt and dR/dt are given by (13). The solution of (30) was obtained numerically and a discussion of the procedure is given in §7.

At this stage the formulation of the unsteady boundary-layer problem is complete. A wide variety of different cases could be considered corresponding to different initial locations of the vortex ring. However, since the computed cases were tied closely to the experiments, it is useful at this stage to describe the experimental apparatus and results.

4. Experimental apparatus

The experiments reported in this study were carried out in the water-channel-flow facility located in the Fluid Dynamics Research Laboratory of Lehigh University. This flow facility is an open-surface water channel which is essentially the same as that described by Smith & Metzler (1983) but suitably adapted for the present study. Figure 4 illustrates the general arrangement of the vortex-ring generator, the video viewing equipment and the lighting.

Single vortex rings were produced in a conventional way by ejecting slugs of fluid through a circular sharp-edged orifice. Upon ejection, the moving body of fluid rolled up into a vortex ring (or more precisely into the shape of an oblate spheroid) which subsequently descended toward a flat plate mounted above the floor of the channel. In the experiments described here the water in the channel was initially stagnant prior to the introduction of the vortex ring.

The vortex-ring generator is shown schematically in figure 5; it is powered by a 0.044 horsepower, variable speed, reversible, direct current electric motor connected to a ball-bearing lead screw by an electric clutch. The lead screw converts the rotary motion of the motor to linear motion of a piston via a constant velocity cam follower mechanism; movement of the piston then pushes fluid out of the orifice. As shown in figure 4, the generator is attached to a traversing platform which is mounted above the water surface; the piston cylinder, the orifice tube and orifice were all submerged below the water surface. All parts exposed to the water were constructed from PVC plastic in order to resist corrosion.

The vortex generator was designed with interchangeable parts which allow the

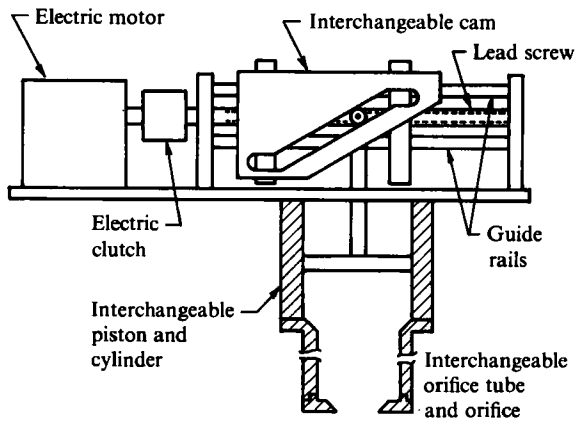

FIGURE 5. Vortex-generator apparatus.

generation of vortex rings with a broad range of characteristics. The motor speed is continuously variable up to 7400 rev/min. Cams having stroke lengths of 0.64, 1.27, 1.9 and 2.54 cm were used; in addition stroke lengths between these values could also be obtained by adjustment of electrical and mechanical stops (not shown in figure 5). The piston stroke length was monitored by a Linear Variable Displacement Transducer (LVDT). Piston diameters of 1.9, 2.54, 3.81 and 5.08 cm and orifice diameters of 0.95, 1.43, 1.90, 2.22, 2.54, 3.18 and 3.81 cm were used.

Let L_M denote the length of the cylindrical slug of fluid ejected from the orifice, D_M the orifice diameter and H_M the height of the orifice from the flat plate near the floor of the channel. For the experimental studies, variation of stroke length, piston size, orifice diameter and orifice tube length allowed the examination of L_M/D_M ratios from 0.75 to 3.41 and H_M/D_M ratios from 2.85 to 6.8. Note that the capability to vary the H_M/D_M ratio was believed to be important since the vortex ring must have sufficient distance to fully form (or roll-up) before it encounters the wall. Saffman (1975) suggests that roll-up is not complete until the ring has moved a distance on the order of several ring radii away from the orifice. Similarly, Sallet & Widmayer (1974) estimate that vortex rings are fully developed once they have moved three diameters away from the generation orifice. In all of the experiments particular care was taken to ensure that each vortex ring was fully developed before it was sufficiently close to the surface to be significantly affected by the wall.

The principal measurable quantities which characterize the fully developed vortex rings are the initial vortex-ring diameter D_0, the initial ring velocity V_0, and the initial Reynolds number Re_0. Here $Re_0 = V_0 D_0/\nu$. All results reported in this study were obtained with laminar vortex rings which were stable prior to impact with the surface.

In order to evaluate all the flow characteristics of interest for a particular vortex ring, it was necessary to perform multiple observations for each set of vortex-ring parameters. Consequently, the vortex generator had to have the capability of producing a series of rings with identical characteristics. The repeatability of the generator was tested by configuring the generator to produce a vortex with a particular set of characteristics for at least two different times during the course of the experimental program, between which the generator had been reconfigured to produce other vortex rings. The characteristics of the fully developed vortex ring such as ring diameter, translational speed and initial Reynolds number were evaluated for

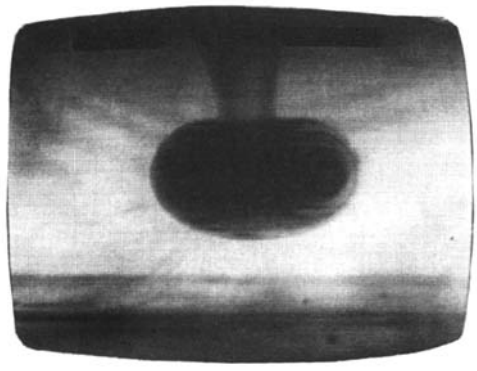

FIGURE 6. Vortex ring approaching a solid plane surface (side view, dye placed in vortex ring). Vortex propagating from the top to the bottom of the picture. $Re_0 = 560$.

each situation and were found to be repeatable to within $\pm 4\%$, $\pm 1\%$, and $\pm 4.5\%$ respectively. These values fall well within the experimental measurement errors of $\pm 7\%$, $\pm 10\%$, and $\pm 11\%$ in the respective quantities; a detailed uncertainty analysis for the data is given by Cerra & Smith (1983). To further assess the repeatability of the generator, the interaction of the vortex ring with the fluid adjacent to the plane wall was observed qualitatively for each case and found to be very similar (if not identical).

Flow visualization as the vortex ring approached the wall was accomplished using two different, but complementary methods of dye injection. In the first method, dye was injected into the fluid within the vortex-generator orifice tube just prior to the generation of a vortex ring; figure 6 shows a typical ring visualized by this method. The particular dye used was a 1:10 mixture of blue food colouring and water; the blue colour was determined to provide a better contrast than other available colours. The specific gravity of the dye mixture was 1.0014; in subsequent tests, 0.6% alcohol (by volume) was added to the dye mixture to decrease the specific gravity of the dye mixture to that of water. No discernible changes in the results were observed. The placement of dye in the primary vortex ring is an effective means for visualizing the initial flow interactions of the ring with the fluid adjacent to the plane surface. However, as the interaction progresses, the dye in the ring was observed to become more diffuse, which made the motions of the deformed ring progressively more difficult to distinguish. In addition, with this method the reaction of the fluid initially adjacent to the surface could only be inferred by observations of the deformation of the primary vortex ring.

To allow observation of the reaction of the fluid in the unsteady boundary layer on the plane wall, a sheet of fluid immediately adjacent to the plane surface was marked with dye; the dye sheet was initialized by slowly injecting dye over a region of the surface using an elongated needle and hypodermic syringe. When this dye-sheet technique was used, the primary vortex ring was not marked with dye; consequently the interior of the primary ring was not visible, and only the outline of the vortex and the induced effects of the vortex on fluid adjacent to the surface were observed. The main advantage of the dye-sheet technique is that it allows clear observation of the behaviour of the fluid in the boundary layer near the wall as well as the subsequent interaction of the boundary-layer fluid with the primary vortex. Clearly, each visualization method is suited to a different purpose; however, because of the

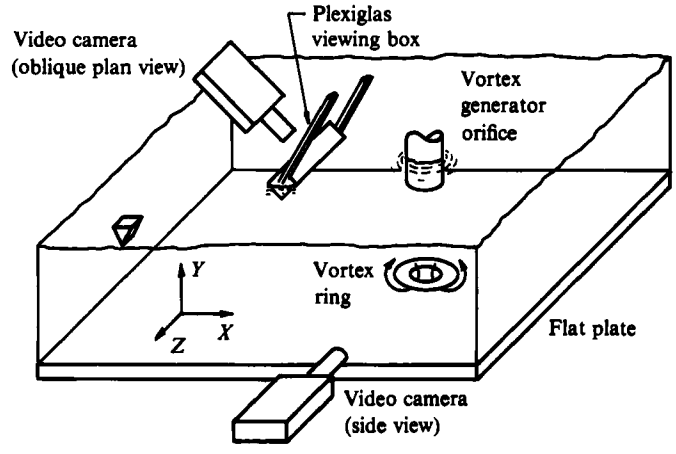

FIGURE 7. Perspective view of camera viewing angles and coordinate system orientation.

consistent repeatability of each experiment, it is possible to compare the results from both approaches to obtain a clear picture of the overall flow field.

As each experiment progressed, it was viewed and recorded using a two-camera INSTAR high-speed video system manufactured by Video Logic Corporation. Framing at a rate of 120 frames/s, the cameras are synchronized with strobe lights to achieve an effective shutter exposure time of 10^{-5} s. The system has a split-screen capability which allows the simultaneous viewing of two different fields-of-view using two different cameras. Videographic data are recorded on a one-inch magnetic tape recording unit and can be played back at real-time forward speeds or in flicker-free forward and reverse slow-motion. Frame-by-frame and stop-action capabilities allow further detailed analysis of the recorded data. Individual pictures from the tapes were obtained using either (i) a videographic copier (a latent image process using heat developed dry silver paper) which interfaces directly with the video recorder or (ii) conventional photographs taken directly from the television screen. The photographs presented in this paper were obtained using the second approach with type 57 Polaroid film and a Polaroid back for a 4×5 Graflex camera.

The two viewing angles employed in the present study are depicted schematically in figure 7. Since the vortex generator obscured conventional plan views of the vortex impact, oblique plan views were taken with the camera offset to the side of the vortex generator, as shown in figure 7. In order to obtain a sharp oblique plan-view, a Plexiglas viewing box was used to prevent the distortion caused by the diffraction of light at the water surface. The lighting equipment consisted of two 90 watt and one 1000 watt strobe lights (synchronized with the cameras) and two auxiliary quartz studio lamps which were used for difficult lighting situations. A white plastic background with backlighting was used during recording, with the strobe lights mounted as depicted in figure 4.

In the present study, sixty-two different sets of physical parameters were considered, allowing examination of laminar vortex-ring impacts having initial Reynolds numbers ranging from 105 to 3000. The visual data recorded included video sequences taken for both qualitative observation of the flow behaviour and for quantitative evaluation. In all, four hours of video tape were recorded, consisting of 1800 separate vortex sequences.

5. Flow visualization results

A typical trajectory of a vortex ring as predicted by inviscid theory has been given in figure 3 (as the solid line); as the ring approaches the wall, inviscid theory indicates that the primary radius of the ring will expand without bound and that the core moves closer and closer to the wall. In the experiments described in this paper, the trajectory of the ring began to depart substantially from the predictions of inviscid theory as soon as the ring was close to the wall. In particular the rate of increase in ring diameter slows significantly and in some cases the diameter of the primary ring was actually observed to attain a maximum and begin to decrease; in addition, the approach toward the wall is generally arrested and the primary vortex was usually observed to rebound from the surface. The phenomenon that is normally responsible for the observed deviation from inviscid theory is an unsteady separation effect, induced in the boundary layer on the wall by the moving primary vortex. The separation usually culminates in the ejection of a secondary vortex from the boundary layer, which then interacts with the primary ring, giving rise to a substantial divergence from the purely inviscid description of the flow. In this section, the results of the flow-visualization studies are employed to document the generally observed features of the vortex-wall boundary-layer interaction. It should be noted that the sequences that are presented here represent only a small sample of the many video sequences used to draw the conclusions presented in this paper. Each selected sequence contains photographs taken from a particular video sequence; unfortunately, the photographic sequences cannot convey the same degree of physical appreciation of the flow-field development as experienced when viewing the original video sequence in slow-motion replay.

It may be inferred from (15) than when the ratio $Y(t)/R(t)$ is large, the tangential velocity induced near the wall is small. On the other hand, as the ring reaches a height above the surface comparable to the ring radius, the dimensionless tangential flow speed induced near the plane wall becomes $O(1)$; consequently the flow in the unsteady boundary layer begins to develop, progressively strengthening velocities as the vortex continues to approach the surface. It may be verified from (15) that at $r = R(t)$ (directly below the core of the moving vortex ring) a velocity maximum occurs near the wall, corresponding to an instantaneous pressure minimum. Outboard of the moving vortex core, the pressure increases radially outward; consequently the boundary-layer fluid outside the moving vortex core is continually exposed to an adverse pressure gradient and eventually boundary-layer separation occurs near the surface. It is convenient to first discuss in general terms the sequence of observed events, during and after the period when boundary-layer separation is observed.

The separation process initiates in a manner similar to that described by Harvey & Perry (1971) and Walker (1978). A closed region of recirculation appears on the wall in the region of adverse pressure gradient; in the classical theory of bluff-body separation (see, for example, Riley 1975) such an event is termed 'separation'. Once this has occurred, an axially symmetric ring of eddying flow with vorticity of the opposite sign to that of the primary vortex ring develops adjacent to the wall outboard of the perimeter of the vortex ring. Rapid thickening of the boundary layer is then observed in a highly localized region near this wall eddy; this portion of the overall process is depicted schematically in figure 8(*a*). Note that the meaning of the term 'separation' has been controversial and some authors (for example, Sears & Telionis 1975) prefer to reserve the term for the type of event depicted in figure 8(*a*) where an initially thin boundary layer is about to strongly interact with an essentially

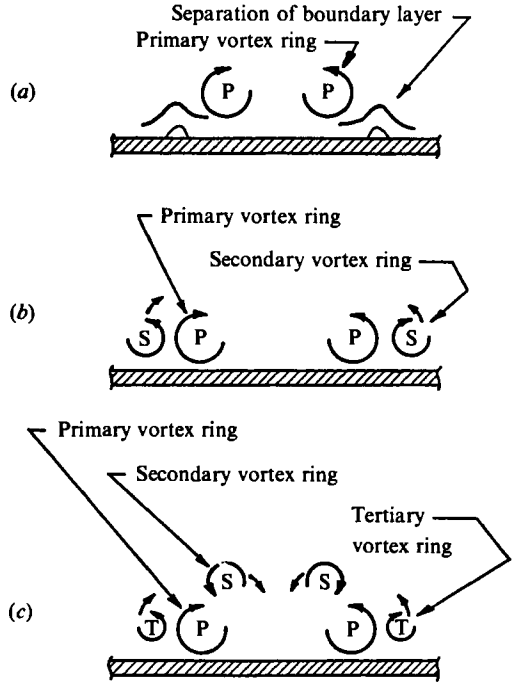

FIGURE 8. Schematic diagram of primary, secondary and tertiary vortex rings: (*a*) primary vortex ring approaching the solid surface and inducing separation in the boundary layer; (*b*) generation of a secondary vortex ring; (*c*) generation of a tertiary vortex ring.

inviscid outer flow. Whether the term separation is used to denote the initial appearance of an eddy of recirculating flow on the wall or to denote the onset of an inviscid–viscous interaction is to some extent a matter of preference; in any case, in the present configuration, the first event is a precursor of the second.

When the original vortex ring is of sufficient strength, the boundary-layer separation culminates in a viscous–inviscid interaction in which a vortex ring of the opposite rotation is ejected from the boundary layer; this event is depicted schematically in figure 8(*b*). To distinguish between the two vortex rings it is convenient to refer to the original vortex ring as the primary vortex ring and to the ring generated from the induced boundary-layer flow as the secondary vortex ring. Once the secondary ring is formed, the primary and secondary rings interact in an apparently inviscid manner which appears to be predictable from the Biot-Savart law. The secondary vortex ring is observed to orbit from the outside perimeter of the primary vortex ring over the top of the core and towards the inside perimeter of the primary ring as indicated in figure 8(*c*). In cases where the primary vortex ring has sufficient strength, after formation of the secondary ring, another vortex ring is observed to form outboard of the primary ring in much the same manner as the secondary ring. This third ring also has vorticity of opposite sign to that of the primary ring and will be referred to as the tertiary vortex ring. A side view showing the typical proximity of these three rings is shown schematically in figure 8(*c*).

With this general discussion of terminology and the overall features of the interaction, it is now possible to examine some specific cases. The detailed features of the process depend on the Reynolds number. A Reynolds number ($Re = \Gamma/\nu$) has

previously been defined in connection with the definitions in (16); here Γ is the circulation associated with the primary vortex ring. Because of the known difficulties (Cerra & Smith 1983) associated with obtaining an accurate and direct measurement of Γ, it proved convenient to define another Reynolds number, based on the initial characteristics of the primary ring, according to

$$Re_0 = \frac{V_0 D_0}{\nu}. \tag{33}$$

Here V_0 and D_0 are the initial translational velocity and diameter of the fully developed primary vortex ring respectively; these quantities were obtained from the video sequences at axial locations on the order of $2.5D_0$ from the orifice of the vortex generator.

For low initial Reynolds numbers corresponding to values of Re_0 less than approximately 250, no secondary or tertiary vortices were observed to form as the primary vortex ring impacts the wall, although a slight rebounding was observed. Apparently, the vorticity of the ring slowly diffuses (Cerra & Smith 1983) with the wall acting as a sink for vorticity. The behaviour observed in such cases is consistent with that reported by Peace & Riley (1983) in their low-Reynolds-number Navier–Stokes calculations for a two-dimensional vortex pair approaching a wall. Peace & Riley (1983) report a slight rebounding of the vortices; however, no separation is observed near the wall, and the vorticity associated with the primary vortices gradually diffuses.

For initial Reynolds numbers, Re_0, greater than approximately 250, the impacting primary ring was observed to induce a separation near the wall; a typical sequence is shown in figure 9 for $Re_0 = 564$. Here only the right-hand half of a dyed vortex ring has been photographed as the ring moves toward the surface. Each picture is of single frames from a video sequence taken 0.25 s apart; the sequence is along each row successively from left to right. The finite increase in the diameter of the marked primary ring may be observed along the first row. The secondary ring is created in the unmarked fluid near the wall and the first hint of its presence may be seen as the indentation in the dyed primary ring in the second photograph in the top row. The process continues into the third photograph; by the fourth photograph in the top row, the outline of the secondary vortex is now visible as dye originally associated with the primary ring has been wrapped around the core of the secondary vortex. Through the second row of photographs, the secondary vortex ring rotates over the core of the primary vortex and its diameter shrinks. The rotation of the end of the dye spiral in the secondary vortex clearly shows the sense of vorticity in the secondary ring. In the third row of photographs, the secondary vortex gradually disappears from view as it orbits into the interior of the primary ring. At the same time, the development of a third, tertiary vortex may be observed outboard of the core of the primary ring.

A plot of the trajectories of the vortex centres for $Re_0 = 564$ is given in figure 10. These trajectories were established from sequences of videographic prints. Repeated viewing of the sequences in slow motion was used in conjunction with the videographic prints to assist in the identification of the centres of the vortex cores. Inviscid theory predicts that the primary vortex ring will asymptotically approach the surface with an ever-increasing diameter; this theory models the behaviour of real vortex rings which are far from the surface. However as the vortex nears the surface, the separation near the wall results in the ejection of the secondary vortex ring from the

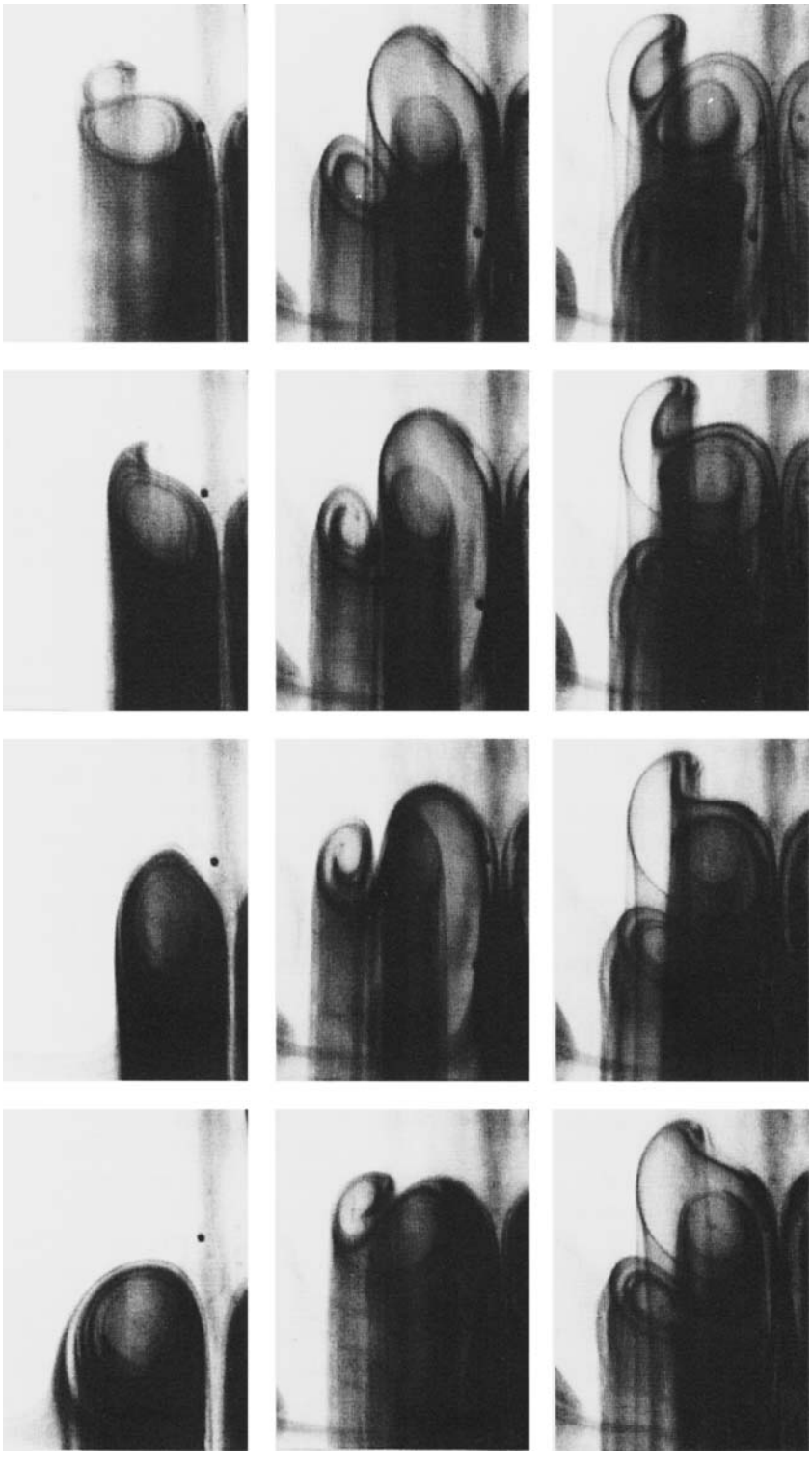

FIGURE 9. Close view of right half of vortex ring impacting solid plane surface (side-view, dye placed in vortex ring). Pictures are 0.25 s apart. $Re_0 = 564$.

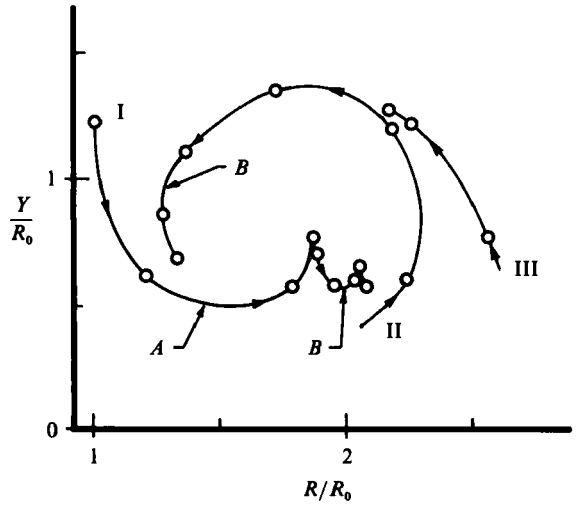

FIGURE 10. Trajectories of the cores of the primary, secondary and tertiary vortex rings for $Re_0 = 564$. Curve I: trajectory of the primary vortex ring. Curve II: trajectory of the secondary vortex ring; point A on curve I coincides in time with the origin of curve II; point B on curves I and II coincides in time with the origin of curve III (the trajectory of the tertiary vortex); O, time intervals of 0.5 s.

wall region which in turn causes an alteration of the motion of the primary ring. Since the secondary ring has the opposite sense of circulation to the primary ring, in a primarily inviscid interaction the flow induced by the secondary ring acts to slow the radial outward motion of the primary ring and also to cause the primary ring to rebound from the wall. In turn, the secondary ring is convected by the velocity field induced by the primary ring toward the centre of the primary ring. At a later stage, the primary ring induces a further separation and boundary-layer eruption in the form of a tertiary vortex which precipitates a second rebound of the primary vortex. Note that the formation of secondary and tertiary vortices occurs near points in the primary trajectory when the primary vortex is closest to the wall. In addition, a finite limit to the radial growth of the primary ring diameter may be clearly observed in figure 10.

For cases with Re_0 less than approximately 600, rebounding of the primary vortex was observed which was accompanied by a dramatic diminution of the outward radial motion of the primary core. As Re_0 was increased, the strength of the spawned secondary vortex relative to that of the primary vortex appeared to increase to the extent that reversals in the radial velocity of the primary ring were observed. This feature is illustrated in figure 11, where the trajectories of the primary vortex are plotted for Reynolds numbers ranging from $Re_0 = 564$ to 2840. At the lowest Reynolds number, only rebounding of the primary vortex occurs; each of the other three trajectories is for an Re_0 in excess of 1300 for which reversal of the radial motion of the primary vortex, as well as rebounding, were always observed. It may be seen from figure 11 that the strength of reversal of the primary vortex, as well as the complexity of the trajectory, increases with increasing initial Reynolds number Re_0.

The physical explanation for the rebounding and the reversals observed in the trajectories of the primary vortex ring appears to lie in the velocities induced by the presence of the secondary and tertiary vortices. As the primary vortex approaches

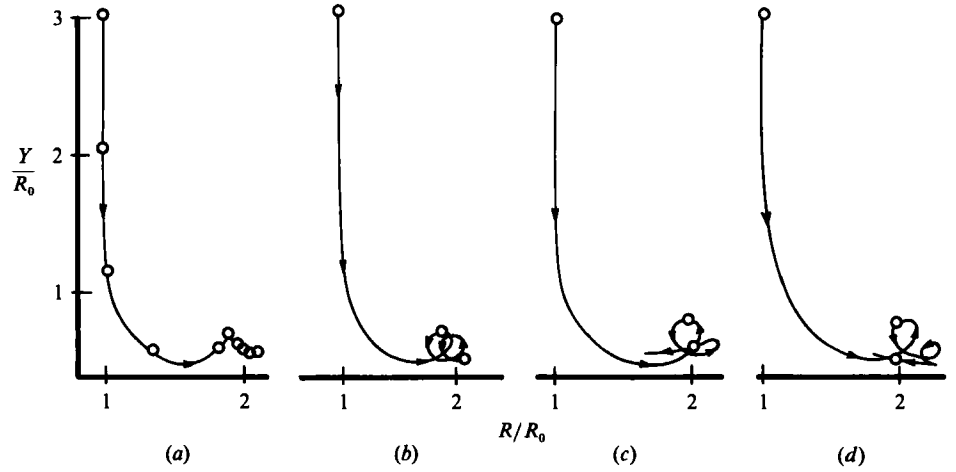

FIGURE 11. Trajectories of the right cores of the primary vortex rings (*a*) $Re_0 = 564$, (*b*) $Re_0 = 1680$, (*c*) $Re_0 = 2550$, (*d*) $Re_0 = 2840$; ○, time intervals of 0.75 s.

the wall, it experiences a radial velocity due to the image vortex below the surface, as well as a self-induced axial propagation velocity. However, the creation of a secondary vortex through an unsteady separation effect near the wall creates a situation where the secondary and primary vortices induce further velocities on one another. It is these velocities which are responsible for the rebounding and reversal in the trajectory of the primary vortex; likewise, the secondary vortex orbits the primary vortex in response to the induced velocity field of the primary vortex. Once the creation of the secondary vortex has occurred, the interaction between the two vortices is essentially inviscid and in principle may be estimated from the Biot-Savart law.

It may be inferred that the secondary vortex will always cause the primary vortex to rebound. For a reversal in the primary trajectory to occur, the secondary vortex ring must be strong enough to cause at least an instantaneous inversion of the radial velocity of the primary ring. In figure 11(*b*), the first reversal is caused by the secondary vortex ring and is only momentary, creating a loop in the trajectory. The second reversal is caused by the tertiary vortex ring; this reversal is also brief and results in a second loop in the trajectory. The primary ring then apparently continues to increase in diameter; however, at this stage, three-dimensional effects begin to have a dominant effect in the flow field and it is not possible to track the evolution of the primary vortex further. For the cases at higher Reynolds numbers in figures 11(*c*) and 11(*d*), the trajectories end up in a state of permanent reversal. This permanent reversal occurs because the tertiary vortex is sufficiently strong and because of a complex interaction that occurs between the three vortex rings.

As the Reynolds number Re_0 increases, wavy instabilities are observed to occur in the secondary vortex. In figure 12, a sequence of photographs is shown for a marked ring at $Re_0 = 1250$ impacting the wall. In the sequence in the first column, the secondary vortex forms and orbits over the primary vortex. In the second column the secondary vortex moves toward the interior of the primary ring and a tertiary vortex may be seen on the outside of the primary ring. However, it may also be seen that a waviness develops in the secondary vortex ring and as time increases the three-dimensionality becomes more pronounced. The same development may be seen

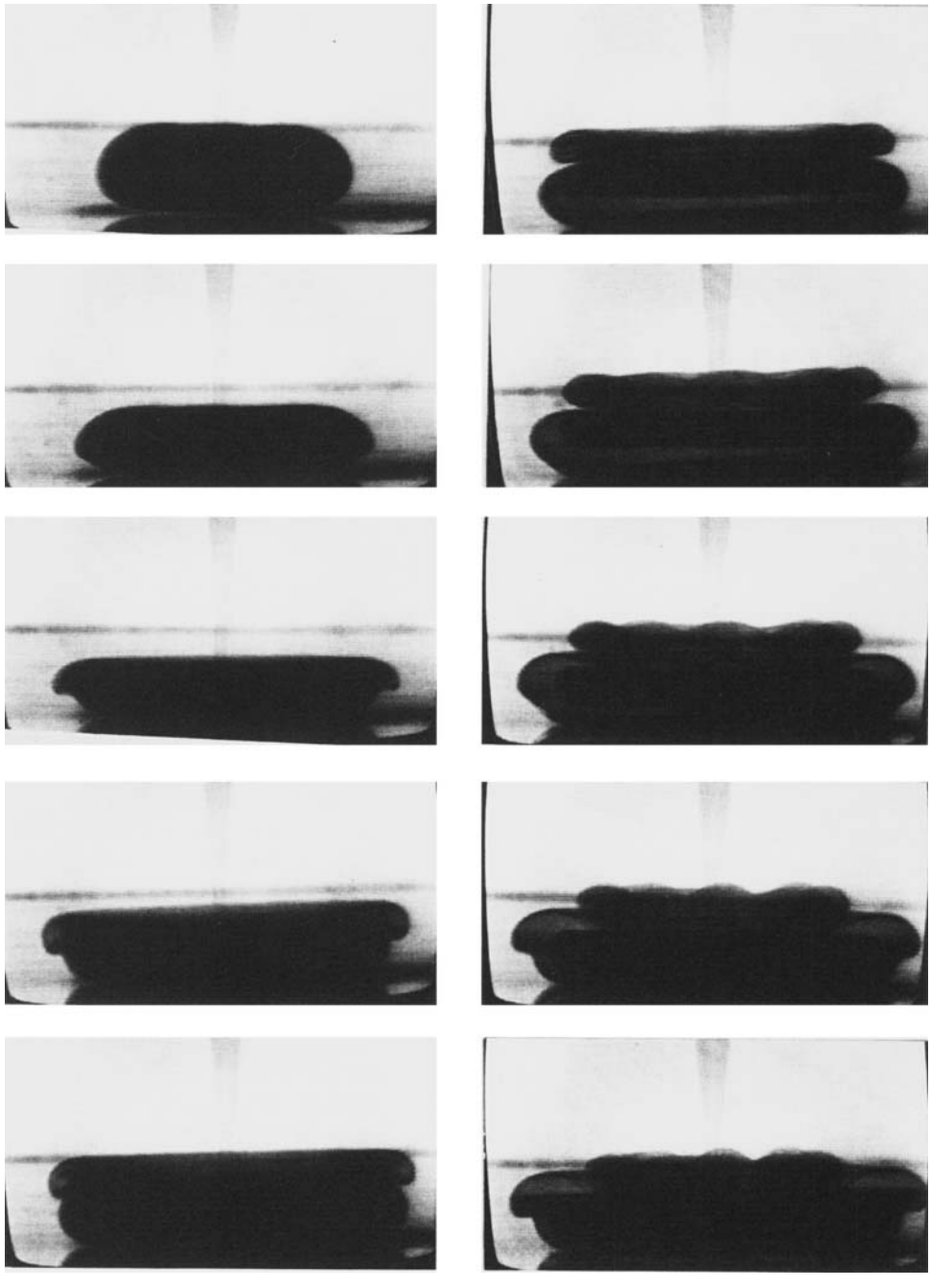

FIGURE 12. Vortex ring impacting solid plane surface (side view). Illustrates development of azimuthal waviness in secondary vortex, visualized by placing dye in vortex ring. $Re_0 = 1250$. Pictures are 0.083 s apart.

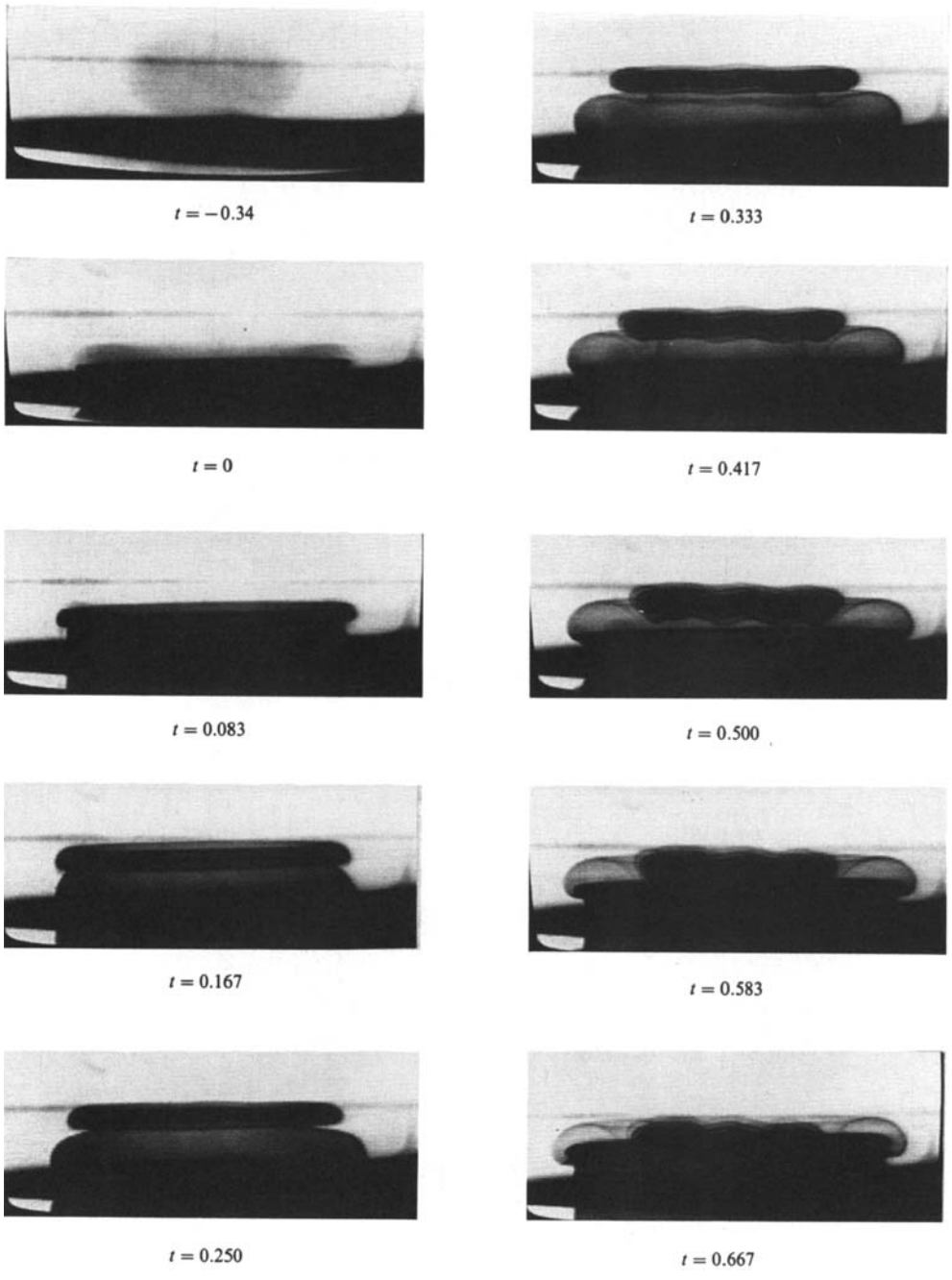

FIGURE 13. Vortex ring impacting solid plane surface (side view). Illustrates development of azimuthal waviness in secondary vortex, visualized by placing dye on the surface. $Re_0 = 1250$. Picture time units are seconds.

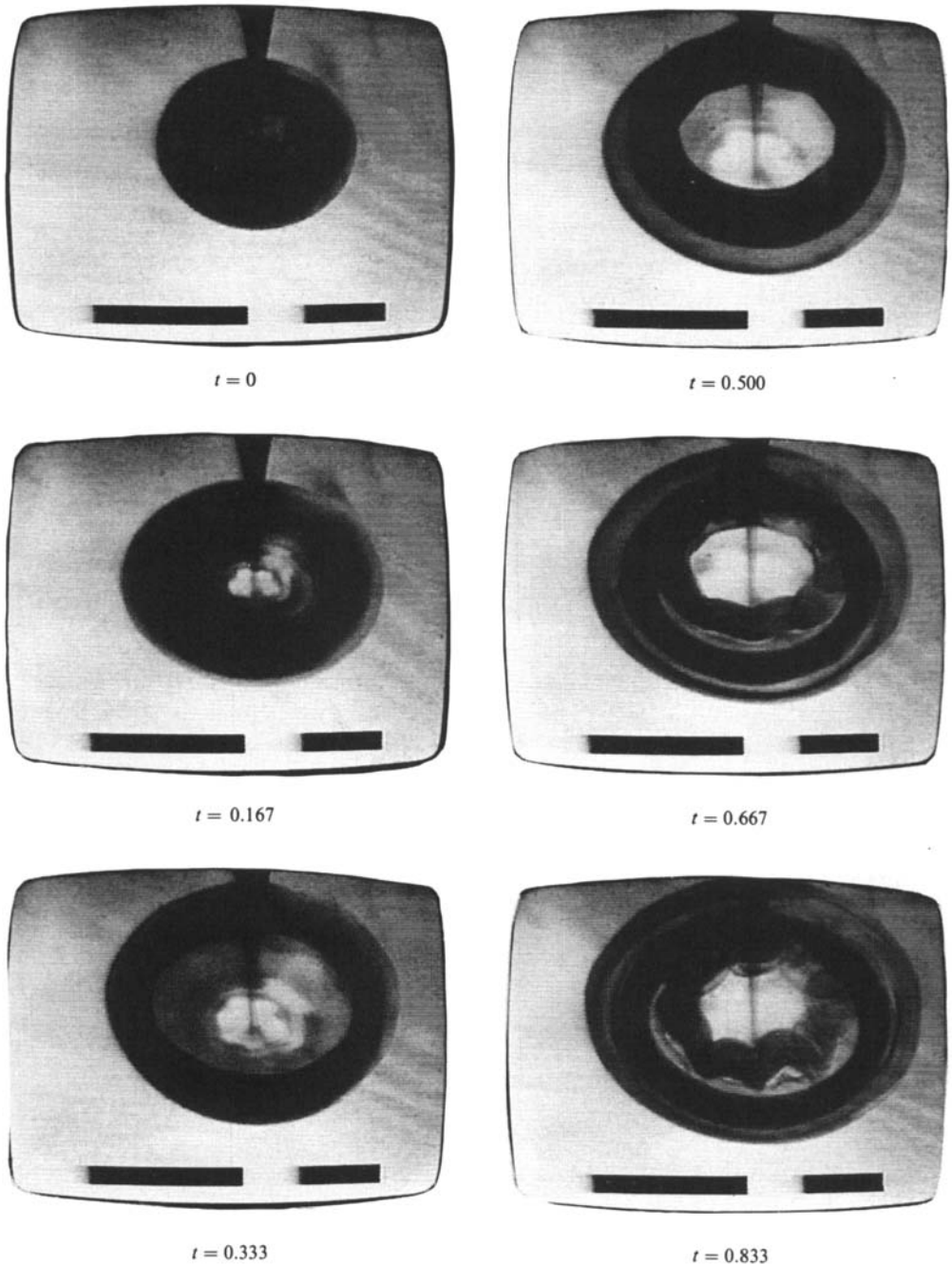

FIGURE 14. Vortex ring impacting solid plane surface (oblique plan view, dye placed in vortex). Illustrates development of azimuthal waviness in secondary vortex. $Re_0 = 1250$. Picture time units are seconds.

from a different perspective in figure 13. In this sequence of photographs, the fluid near the wall has been marked with dye and the primary vortex is only weakly marked. As the secondary vortex forms and rotates into the interior region of the primary ring, the primary ring appears to be ensheathed with a dye sheet. Upon comparing figures 12 and 13, it is evident that the secondary vortex contains fluid originally from the primary vortex as well as from the originally quiescent fluid near the plate.

A third perspective in oblique plan-view for this case is provided in figure 14 for the dyed primary vortex. Note that the amplitude of the azimuthal waves, which develop on the secondary vortex, increases with time. It is well known (Widnall & Sullivan 1973) that a vortex ring propagating through an otherwise quiescent fluid can develop an instability which leads to the development of an azimuthal waviness in the ring. Whether or not the instability occurs depends on the vortex Reynolds number, as well as the distance travelled, with larger values of either of these quantities implying that the development of an instability is more likely. The present experiments were configured so that the primary rings remained stable prior to impact. Of the many vortices generated, a few developed the azimuthal waviness in the primary ring prior to impact with the wall region; however, the vast majority appeared to be stable and axially symmetric upon reaching the wall region. In fact, it may be observed in figures 12 and 13, that the initially stable primary ring does not display any azimuthal distortion even after the secondary vortex has developed extreme azimuthal waviness. The instability thus appears to be initiated in the secondary vortex and is believed to be associated with compression of the secondary vortex as it orbits into the interior of the primary vortex. The instability in the secondary vortex was observed to ultimately induce an apparent waviness in the primary vortex; this process was then observed to lead to a degeneration of the flow field into a truly three-dimensional state. The scales of the motion were observed to continually decrease until an apparently chaotic 'turbulent' state occurred. The development of this azimuthal loop instability on the secondary vortex is complex and is documented elsewhere (Cerra & Smith 1983).

For the Reynolds number range of $Re_0 = 470$ to 1600, the wavy-loop type of instability was invariably observed to occur in the secondary vortex. The range between 1600 and 2500 appears to be a transition zone to another type of instability which Cerra & Smith (1983) have termed a kink instability. An example of this type of instability may be seen in figure 15 which is a sequence of oblique plan-view photographs for $Re_0 = 2550$. The secondary vortex forms in the same manner as for the lower Reynolds numbers; it then develops a weak azimuthal waviness which does not increase in amplitude once the secondary vortex orbits into the interior of the primary ring. The secondary vortex then appears to pause for some time within the interior of the primary ring until the tertiary vortex ring develops and orbits to a position above the primary ring; this process may be seen in figure 15 in the interval from $t = 0.308$ to $t = 0.475$. At this point, a rapid ejection of the secondary ring was observed and the secondary ring moved quickly away from the plate, dragging the tertiary ring with it. A typical side view of this process is shown in the sequence in figure 16 for $Re_0 = 3000$. Note the mushroom cloud caused by the abrupt ejection of the secondary ring, and the rapid degeneration of the flow to an apparently 'turbulent' state. The trajectories for a typical case in this Reynolds number range are shown in figure 17. It may be observed that there are two occurrences of rebounding and reversal of the primary vortex before ejection of the secondary vortex

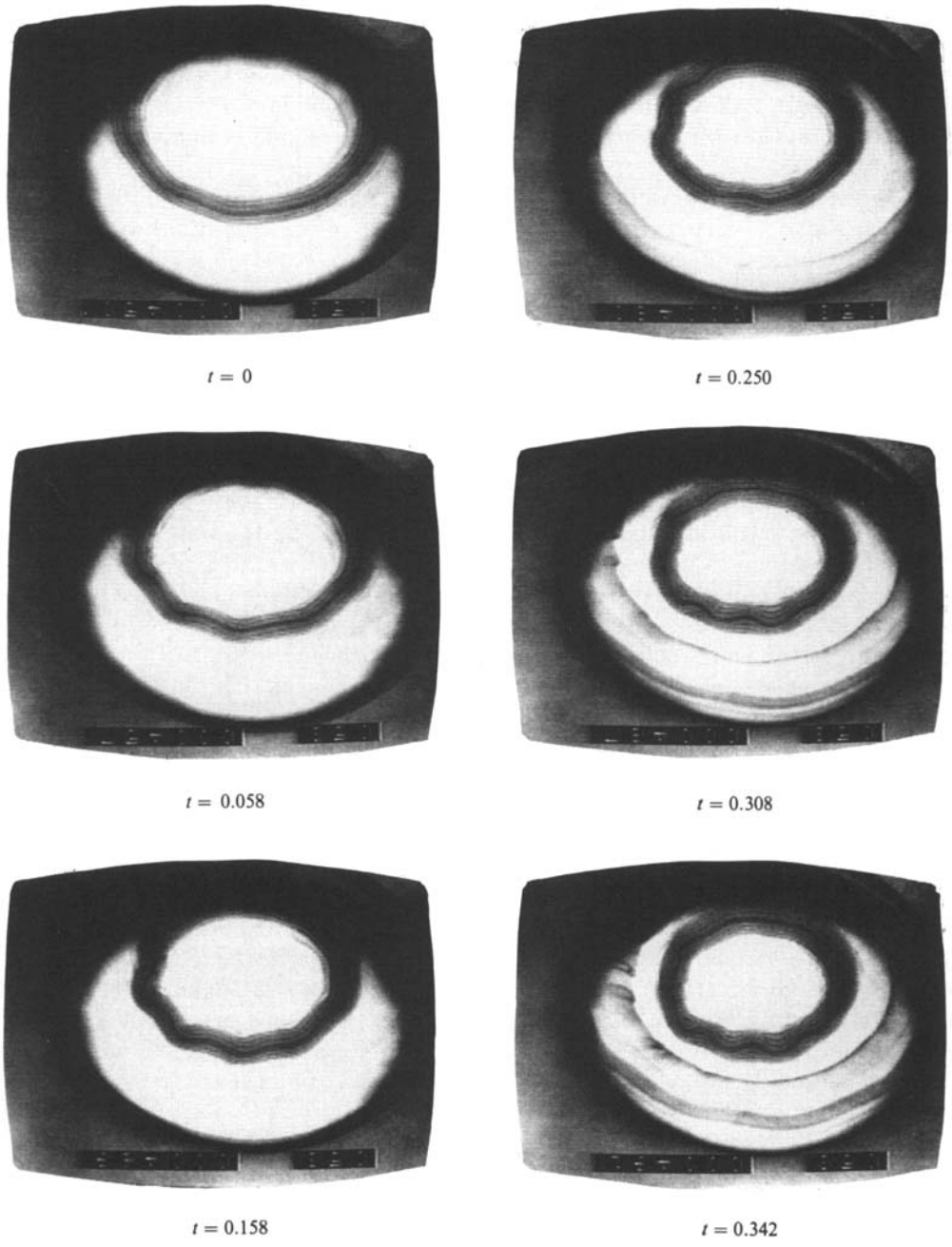

FIGURE 15(a). For caption see facing page.

occurs. The flow development in this Reynolds number range is complex and is discussed in detail elsewhere (Cerra & Smith 1983).

A value of $Re_0 = 3000$ represents an upper limit for the vortex interactions considered in this study. Beyond this value it was not possible to consistently produce laminar primary vortices which remained stable as they approached the wall region.

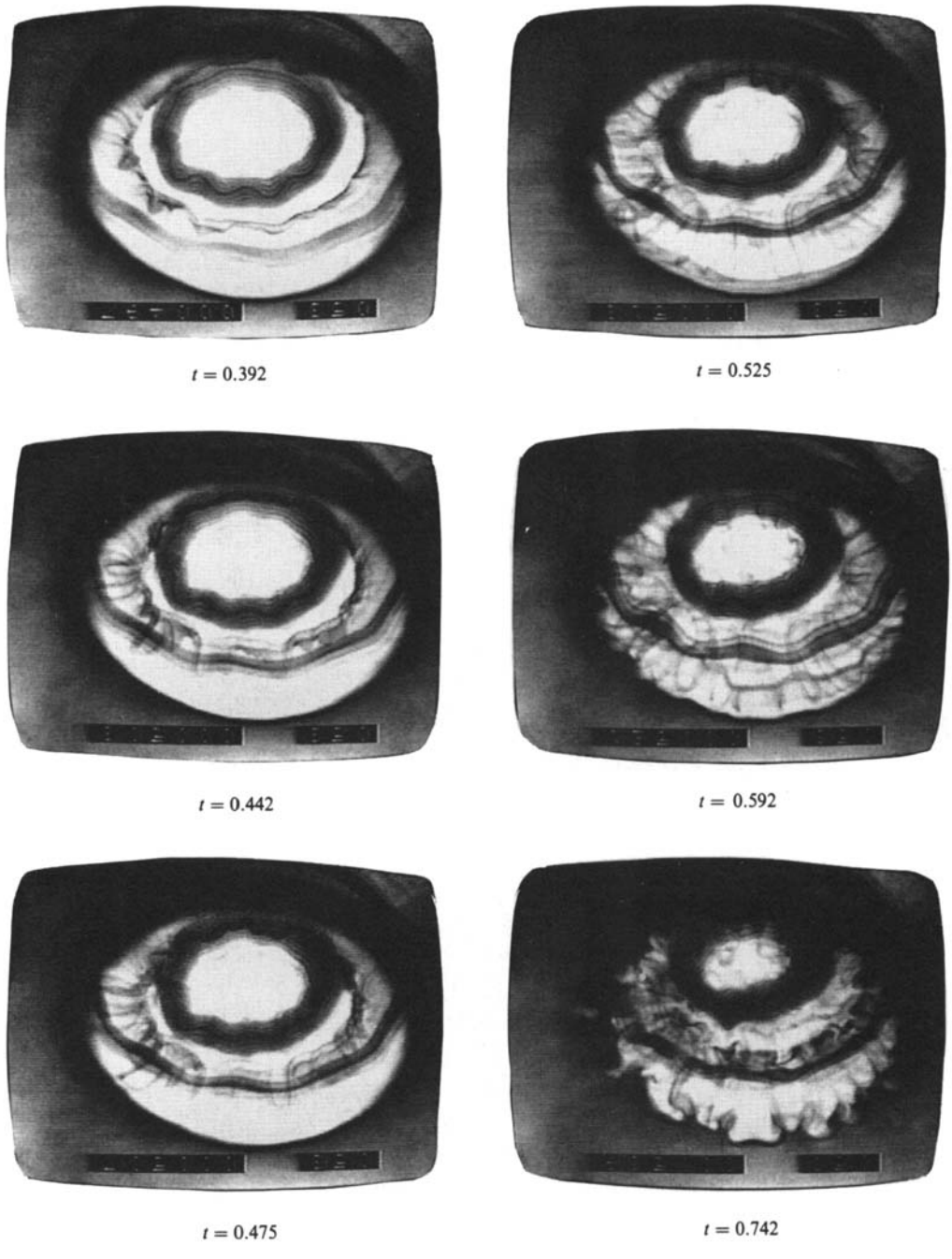

FIGURE 15. Development of kink structures secondary vortex with secondary vortex ejection. Visualized by placing dye on the surface (oblique plan view). $Re_0 = 2550$.

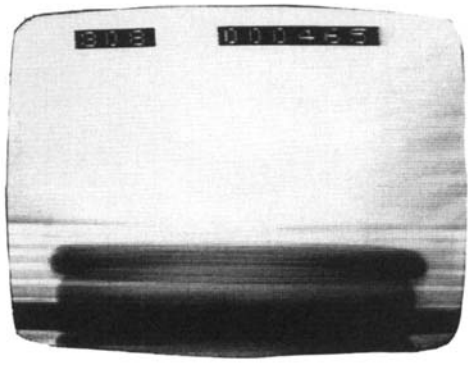

$t = 0$

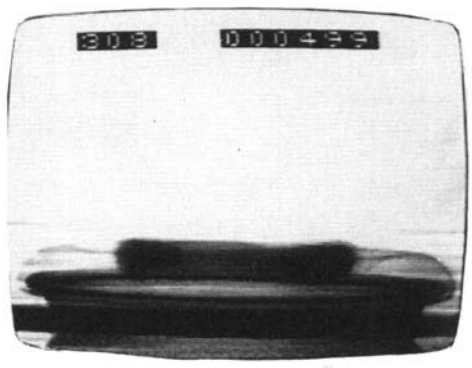

$t = 0.283$

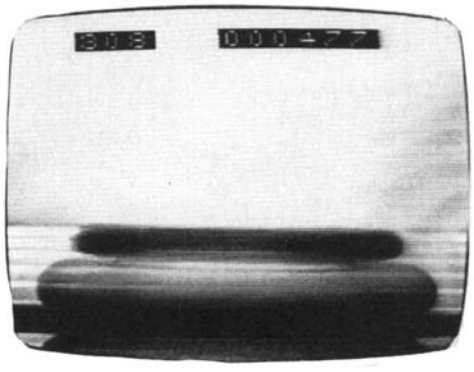

$t = 0.100$

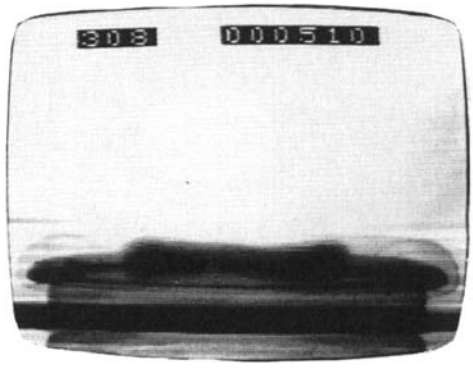

$t = 0.375$

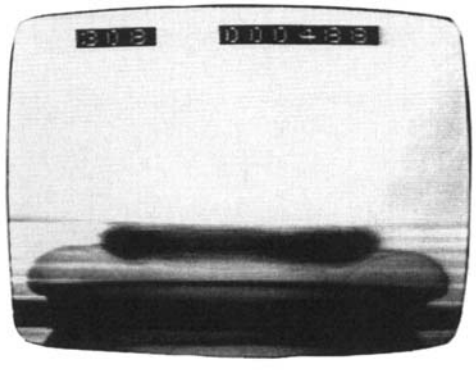

$t = 0.192$

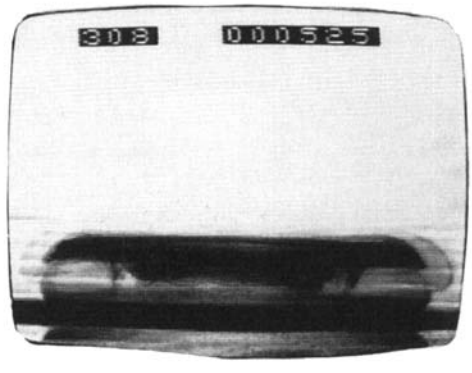

$t = 0.492$

FIGURE 16(*a*). For caption see facing page.

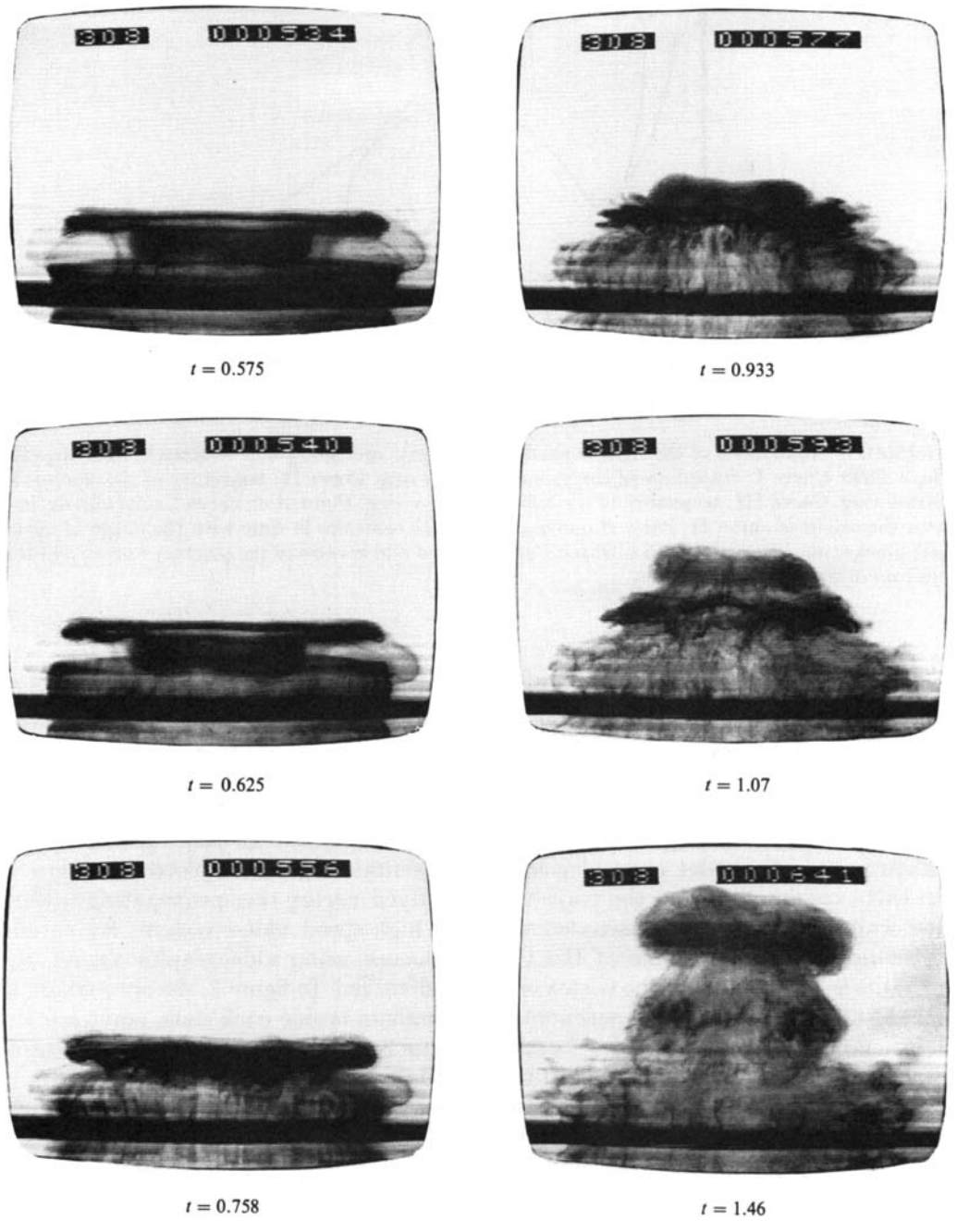

FIGURE 16. Development of kink structured secondary vortex with secondary vortex ejection (side-view, dye placed on surface). $Re_0 = 3000$.

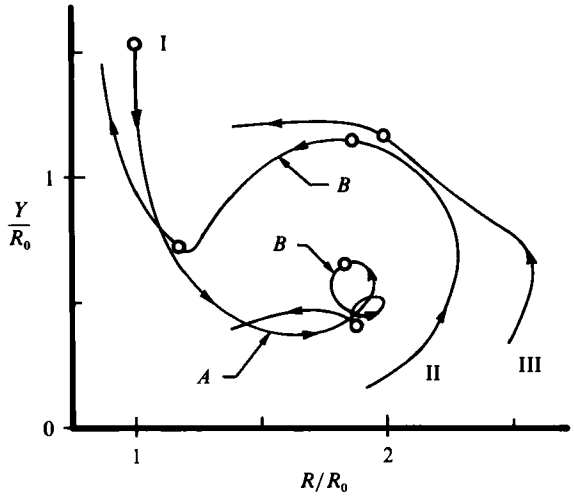

FIGURE 17. Trajectories of the right cores of the primary, secondary and tertiary vortex rings for $Re_0 = 2840$. Curve I: trajectory of the primary vortex ring. Curve II: trajectory of the secondary vortex ring. Curve III: trajectory of the tertiary vortex ring. Point A on curve I coincides in time with the origin of curve II. Point B on curves I and II coincides in time with the origin of curve III; marks time intervals of 0.5 s. Observe the rebound and reverse of the primary vortex and the ejection of the secondary vortex.

6. Numerical solution for the ring trajectory

In order to calculate a numerical solution of the ring trajectory as predicted by inviscid theory, it is necessary to integrate (13). With reference to (6) and (12), it may be seen that in order to initiate the integration it is necessary to specify the initial location of the core of the ring (R_0, Y_0) and the constant C in (11) and (12). In order to compare with the experimental results, values selected for (R_0, Y_0) and C were taken from a particular video sequence, the results of which are plotted in figure 3. In this experimental run, the trajectory of a dyed vortex ring propagating toward the wall was viewed and recorded with the high-speed video system. By careful examination of each frame of the video sequence using videographic prints, the instantaneous location of the vortex core was identified. In figure 3, the open triangles are data points from the experiment; the numbers beside each data point are the frame numbers from each video frame. In figure 3, only data from every fifth frame have been shown; the time interval between data points is $\frac{1}{24}$ seconds.

The process of vortex-ring formation by the ejection of a finite slug of fluid through an orifice has been discussed by Saffman (1975) who points out that the roll-up process is not generally complete until the ring has moved several ring radii away from the orifice. In accordance with this observation, the initial position (R_0, Y_0) that was used in the numerical integration was taken directly from the experimental data at frame 460, which corresponded to a vertical distance from the orifice of the generator approximately 2.5 times the initial ring radius. Note that in the preceding frames (450 to 460) the ring appears to be contracting in radius.

To obtain a representative value for the volumetric constant C defined in (11), a fixed horizontal hydrogen bubble wire was placed in the water channel in such a location that the vortex ring would convect over it. The wire was positioned at various vertical locations between those indicated by frames 460 to 490 in figure 3;

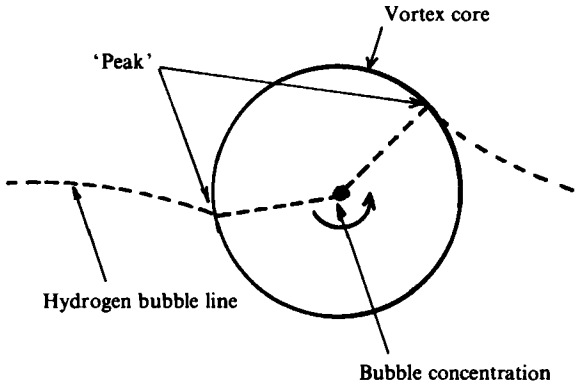

FIGURE 18. Schematic sketch of the hydrogen bubble line (indicated by the dashed line) used to estimate the vortex core size.

the wire was pulsed just as the vortex ring reached the immediate vicinity of the wire to produce a line of hydrogen bubbles in the flow. As the ring convects past the bubble wire two 'peaks' are produced in the bubble lines as sketched in figure 18. These peaks correspond to the location where the angular velocity about the vortex core is largest. Note that the peak on the outboard side of the core is relatively pronounced while the peak on the interior side is rather small as indicated in figure 18. The bubbles tend to concentrate in the core of the vortex where the angular velocity is a minimum. An estimate of the core radius $a(t)$ was then obtained by measuring the distance from the peaks to the bubble concentration. An estimate of the constant C may be obtained by directly applying (11), since the corresponding ring diameter may readily be evaluated from the video sequences. For the particular sequence depicted in figure 3, a value of $C = 3.33 \times 10^{-2}$ cm^3 was obtained in the manner described.

With the initial position (R_0, Y_0) corresponding to frame 460 in figure 3 and the empirically determined value of C, equations (13) were integrated numerically forward in time using a fourth-order Runge–Kutta method. A series of calculations using very small timesteps were carried out to ensure that the numerical error in this procedure was negligibly small. The predicted trajectory is shown in figure 3, where it may be observed that there is relatively good agreement with the experimental results. The fluctuations in ring diameter between frames 460 and 525 are well within the experimental error. In order to compare with the initial data points, the numerical solution was extended back to a time prior to that corresponding to frame 445. The initial behaviour of the ring (frames 445–460) may be attributed to the effects of the generator nozzle and bears a resemblance to the fluctuations observed by Maxworthy (1977) in the vicinity of the generator orifice. It may be inferred from the data points corresponding to frames 530 and higher that the ring is rebounding from the plate and deviating progressively from the trajectory predicted by inviscid theory. This behaviour is due to the production of the secondary vortex discussed in the previous section.

One point of interest concerns the circulation of the ring Γ. Since Γ has been scaled out of the velocities and time (in defining dimensionless variables), the shape of the trajectory is independent of circulation. The particular value of Γ influences only the rate at which the vortex ring moves along the trajectory in figure 3. The direct experimental measurement of Γ is a very difficult problem which has been discussed by a variety of authors (Sullivan, Widnall & Ezekiel 1973; Maxworthy 1977; Didden

1977; Brasseur & Chang 1981; Cerra & Smith 1983) who have suggested a variety of techniques. The merits of these approaches will not be discussed here but the reader is referred to a careful comparison and critical discussion of the techniques in Cerra & Smith (1983). It emerges that discrepancies of the order of 50 % are not uncommon in comparing two methods of directly measuring Γ. In the present study, one objective was to obtain a comparison between predicted and observed separation times in the boundary layer, and to facilitate this comparison, an estimate of Γ was required. This estimate was obtained indirectly by using the formula for the self-induced velocity of a vortex ring; in dimensional form the self-induced velocity U_s is given by

$$U_s = \frac{\Gamma}{4\pi LR}\left[\log\left(\frac{8R}{a}\right) - \frac{1}{4}\right], \tag{34}$$

for a ring in which $a/R \ll 1$ and for which the circular core is in a state of solid-body rotation. When the ring is at locations remote from the wall, (for example, at locations corresponding to frames 460 to 500 in figure 3) the influence of the image vortex is small and the speed of the ring will be given by (34). Consequently measurements of U_s, R and a (using the method discussed in connection with figure 18) yield a value of Γ upon substitution in (34). For the trajectory in figure 3, the value of Γ produced by this approach was 17.5 cm^2/s.

It is important to note that there is a variety of assumptions that have been used to arrive at values of C and Γ from the experiments. The core has been assumed circular and in solid-body rotation; other forms of (34) could be considered, corresponding to different distributions of vorticity in the vortex core. In addition, the measurement of U_s, $R(t)$ and particularly $a(t)$ (via the method discussed in connection with figure 18) are subject to error. However, our purpose here is not to attempt to model closely the internal dynamics of the vortex core, but rather to obtain values of Γ and C which are of the correct order of magnitude and which are reasonably consistent with experiment. Note that Γ is not sensitive to the particular value of C assumed in (11): a change of ± 20 % in the empirical value of $C = 0.0333$ cm^3 produces changes of ± 3.5 % in the value of $\Gamma = 17.5$ cm^2/s. With such values in hand it is now possible to consider the detailed nature of boundary-layer development as the ring approaches the wall.

7. Numerical solution of the boundary-layer problem

A solution of (21) and the associated equations (26) and (30) (at the boundaries $r = 0$ and $r \to \infty$ respectively) may be developed by expanding the solution as a power series in time according to

$$\frac{\partial F}{\partial \eta}(r, \eta, t) = \operatorname{erf}\eta + t\frac{\partial \tilde{F}}{\partial \eta}(r, \eta) + O(t^2). \tag{35}$$

This procedure is well known (Blasius 1908) and yields a solution which is valid for small time; to extend the solution to larger times a fully numerical integration of (21) was carried out. However, the first two analytic terms in (35) have been evaluated by Doligalski (1980) and this time-series solution served to provide a basis for comparison of the accuracy of the fully numerical approach in the initial stage of the integration.

Because the range of the radial variable is semi-infinite, it is convenient (for the numerical solution) to introduce a new variable ξ defined by

$$\xi = \frac{1}{\sigma(t)} \int_0^{g(r)} U_\infty(x, t)\, \mathrm{d}x, \quad \sigma(t) = \int_0^\infty U_\infty(x, t)\, \mathrm{d}x, \tag{36a, b}$$

where $U_\infty(r, t)$ is the outer inviscid velocity given by (15) and $g(r)$ is a monotonically increasing function of r (to be selected) with $g(0) = 0$ and $g \to \infty$ as $r \to \infty$. This transformation is one-to-one and compresses the semi-infinite range in r, $[0, \infty)$, to the finite range for ξ of $[0, 1)$. It is easily confirmed that g must be selected so that $g = O(r^{\frac{1}{2}})$ for small r in order that $\xi = O(r)$ as $r \to 0$; on the other hand, in order to maintain the same rate of decay in U_∞ for large r, it is necessary that g be $O(r)$ as $r \to \infty$. A simple choice for g satisfying these criteria is

$$g(r) = (cr + (1-c)r^2)^{\frac{1}{2}}, \tag{37}$$

where c is a constant. The principal effect of transformation (36) is to expand the region which is instantaneously below the core of the vortex ring where rapid boundary-layer growth is expected. One additional feature of (36) is that the vortex core may be located close to the centre of the ξ range during the entire integration; by trial-and-error it was determined that a value of $c = 0.25$ achieved this objective. Note that in the physical space, the radial location of the vortex core increases continuously with time.

Due to the complicated form of the inviscid velocity distribution $U_\infty(r, t)$ given by (15), the integrations in equations (36) were performed numerically at any fixed value of t using a modified Simpson's rule procedure (Dennis & Walker 1971). In this approach, at any given time t a uniform grid spacing in the r-direction was defined, with mesh size $\Delta r = 4 \times 10^{-3}$; the integral on the right-hand side of (36a) was then evaluated for each point in the r mesh. The numerical integrations were carried out using a uniform mesh spacing in the ξ-coordinate; for a given value of ξ in (36), the corresponding value of r (at fixed t) was determined by a process of inverse interpolation of the results of the integration in the r-coordinate.

The unsteady boundary-layer equations (21) may be written as the system

$$\frac{\partial F}{\partial \eta} = U, \tag{38}$$

$$4t \frac{\partial U}{\partial t} = \frac{\partial^2 U}{\partial \eta^2} + \tilde{P} \frac{\partial U}{\partial \eta} + \tilde{R} U + \tilde{Q} \frac{\partial U}{\partial \xi} + S, \tag{39}$$

where the functions in (39) are defined by

$$\tilde{P} = 2\eta + \frac{4tU_\infty(r, t)\, F}{r} + 4tF \frac{\partial U_\infty}{\partial r} + \frac{4tU_\infty(r, t)\, U_\infty(g(r), t)\, g'(r)}{\sigma(t)} \frac{\partial F}{\partial \xi}, \tag{40}$$

$$\tilde{Q} = -4t \frac{\partial \xi}{\partial t} - \frac{4tU_\infty(r, t)\, U_\infty(g(r), t)\, g'(r)}{\sigma(t)} U, \tag{41}$$

$$\tilde{R} = -4t \frac{\partial U_\infty}{\partial r} U - \frac{4t}{U_\infty} \frac{U_\infty}{\partial t}, \tag{42}$$

$$\tilde{S} = \frac{4t}{U_\infty} \frac{\partial U_\infty}{\partial t} + 4t \frac{\partial U_\infty}{\partial r}. \tag{43}$$

In these equations, $\partial U_\infty/\partial t$ and $\partial U_\infty/\partial r$ are to be regarded as known functions of (ξ, t); for a given value of ξ and hence r, both gradients are evaluated by differentiation of (15). The specific expressions are

$$\frac{\partial U_\infty}{\partial r} = -\frac{3}{2r}U_\infty + \frac{k_0}{2r}\frac{(Y^2+R^2-r^2)}{Y^2+(r+R)^2}\frac{\partial U_\infty}{\partial k_0}, \tag{44}$$

$$\frac{\partial U_\infty}{\partial t} = \left(\frac{U_\infty}{Y} - \frac{Yk_0^3}{4rR}\frac{\partial U_\infty}{\partial k_0}\right)\frac{\mathrm{d}Y}{\mathrm{d}t} + \left(-\frac{U_\infty}{2R} + \frac{k_0^3}{8r^2R}(Y^2+R^2-r^2)\frac{\partial U_\infty}{\partial k_0}\right)\frac{\mathrm{d}R}{\mathrm{d}t}, \tag{45}$$

where k_0 is given in (15) and $\mathrm{d}Y/\mathrm{d}t$ and $\mathrm{d}R/\mathrm{d}t$ by (13); in addition

$$\frac{\partial U_\infty}{\partial k_0} = \frac{Yk_0^2}{4\pi R^{\frac{1}{2}}r^{\frac{3}{2}}(1-k_0^2)}\left[\frac{(3-k_0^2)}{1-k_0^2}\{2B(k_0)-E(k_0)\} + k_0\{2B'(k_0)-E'(k_0)\}\right]. \tag{46}$$

Finally in (41), $\partial\xi/\partial t$ may be calculated from

$$\frac{\partial \xi}{\partial t} = -\xi\frac{\sigma'(t)}{\sigma(t)} + \frac{1}{\sigma(t)}\int_0^{g(r)}\frac{\partial U_\infty}{\partial t}\,\mathrm{d}t. \tag{47}$$

The equations (26) and (30), describing the boundary-layer development on the symmetry axis and at large distances from the ring, may also be written in a form similar to (39) according to

$$4t\frac{\partial U}{\partial t} = \frac{\partial^2 U}{\partial \eta^2} + \tilde{P}\frac{\partial U}{\partial \eta} + \tilde{R}U + \tilde{S}. \tag{48}$$

On the symmetry axis ($r = \xi = 0$)

$$U = U_0 = \frac{\partial F_0}{\partial \eta}, \tag{49}$$

and from (26)

$$\left.\begin{aligned} \tilde{P}_0 &= 2\eta + 8\alpha t F_0 \\ \tilde{R}_0 &= -4\alpha t U_0 - \frac{4t}{\alpha}\frac{\mathrm{d}\alpha}{\mathrm{d}t} \\ \tilde{S}_0 &= 4\alpha t + \frac{4t}{\alpha}\frac{\mathrm{d}\alpha}{\mathrm{d}t} \end{aligned}\right\}, \tag{50}$$

where the subscript 0 denotes quantities at $\xi = 0$ and $\alpha = \alpha(t)$ is given by (25). At large distances from the ring ($\xi \to 1$, $r \to \infty$)

$$U = U_1 = \frac{\partial F_1}{\partial \eta}, \tag{51}$$

and from (30)

$$\tilde{P}_1 = 2\eta, \quad \tilde{R}_1 = -4t\frac{d\beta}{\mathrm{d}t}, \quad \tilde{S} = 4t\frac{\mathrm{d}\beta}{\mathrm{d}t}, \tag{52}$$

where the subscript 1 denotes values at $\xi = 1$ and $\beta(t)$ is defined by (29). The boundary conditions for (39) and (48) are

$$U = F = 0 \quad \text{at } \eta = 0, \quad U \to 1 \quad \text{as } \eta \to \infty. \tag{53}$$

The initial conditions are

$$U = U_1 = U_0 = \operatorname{erf}\eta \quad \text{at } t = 0, \tag{54}$$

A mesh in the $\xi\eta$ plane was defined with spacings h_1 and h_2 in the ξ- and η-directions respectively. A number of mesh sizes were used as a check on the accuracy and values

$h_1 = 0.00555$ and $h_2 = 0.0667$ were determined to give accurate results. The last condition in (53) was applied at $\eta = 6$ as an approximation and this value was found to be large enough to ensure that there was no significant effect on the computed results. In the initial stages of the motion, variations with time are relatively intense, and to ensure good accuracy, the timestep was initially taken to be very small. The calculations were initiated with five steps with $\Delta t = 0.001$ until $t = 0.005$; then four steps with $\Delta t = 0.005$ were taken until $t = 0.025$; at this stage, the timestep was increased to $\Delta t = 0.025$ and held constant throughout the integration.

The numerical methods used have been described by Doligalski & Walker (1984). The first method is based on a Crank–Nicolson approach and is second-order accurate in both space directions and in time. At each timestep, the solution of (48) at $\xi = 0$ and $\xi = 1$ was first advanced using a normal Crank–Nicolson method; these computed values then provide boundary conditions at $\xi = 0$ and 1 for the interior problem $(0 < \xi < 1)$. The solution of (39) was then advanced one timestep; the difference equations resulting from the numerical approximations are nonlinear and were solved iteratively using successive-over-relaxation. Typically 15–20 iterations or sweeps of the mesh in the interior were required to obtain convergence; this was considered to have occurred when successive iterates for U agreed to within four significant figures at all internal mesh points. In the latter stages of the integrations, after separation occurs, appreciable normal velocities begin to develop within the boundary layer; the matrix problem associated with the Crank–Nicolson method failed to remain diagonally dominant and the iterative scheme broke down. In this situation, the alternative differencing scheme of Doligalski & Walker (1984) was used; this approach affects only the differencing of the convective terms and results in a matrix problem which is always diagonally dominant. It was found that the alternative differencing scheme could be used to continue the boundary-layer integrations well beyond the point where the Crank–Nicolson scheme failed.

8. Calculated results

The calculation of the inviscid trajectory has been discussed in §6 and the trajectory for a particular case has been plotted in figure 3. To initiate the boundary-layer integrations it is necessary to select an origin of time, and calculations were originally carried out using an initial ring position corresponding to frame 460 in figure 3. However, it emerged that at this location the ring is so far away from the wall that very little boundary-layer development was observed for some time. In fact, in the majority of the experiments little development was observed near the wall until the vortex ring was within a distance from the wall comparable to its diameter. For this reason, it was decided to define $t = 0$ in the experiments as the instant when $Y = 2R$, as a standard and convenient origin from which to measure separation times in the boundary layer. In accordance with this criterion, the numerical integrations were started with an initial configuration corresponding to frame 513 in the sequence depicted in figure 3; for this case, $L = 1.322$ cm and $Y_0 = 1.184$ cm, $R_0 = 0.589$ cm.

In the initial stages of the integrations, the boundary-layer growth rate was still relatively small and the streamline patterns display an expected downward and then upward motion, as depicted in figure 19(*a*) at $t = 1.4$. In figure 19, the instantaneous streamlines have been plotted in the r-coordinate (rather than the ξ-coordinate used in the numerical integrations) to give an undistorted picture of the actual flowfield. In addition, the triangle at the top of the first graph denotes the initial radial location

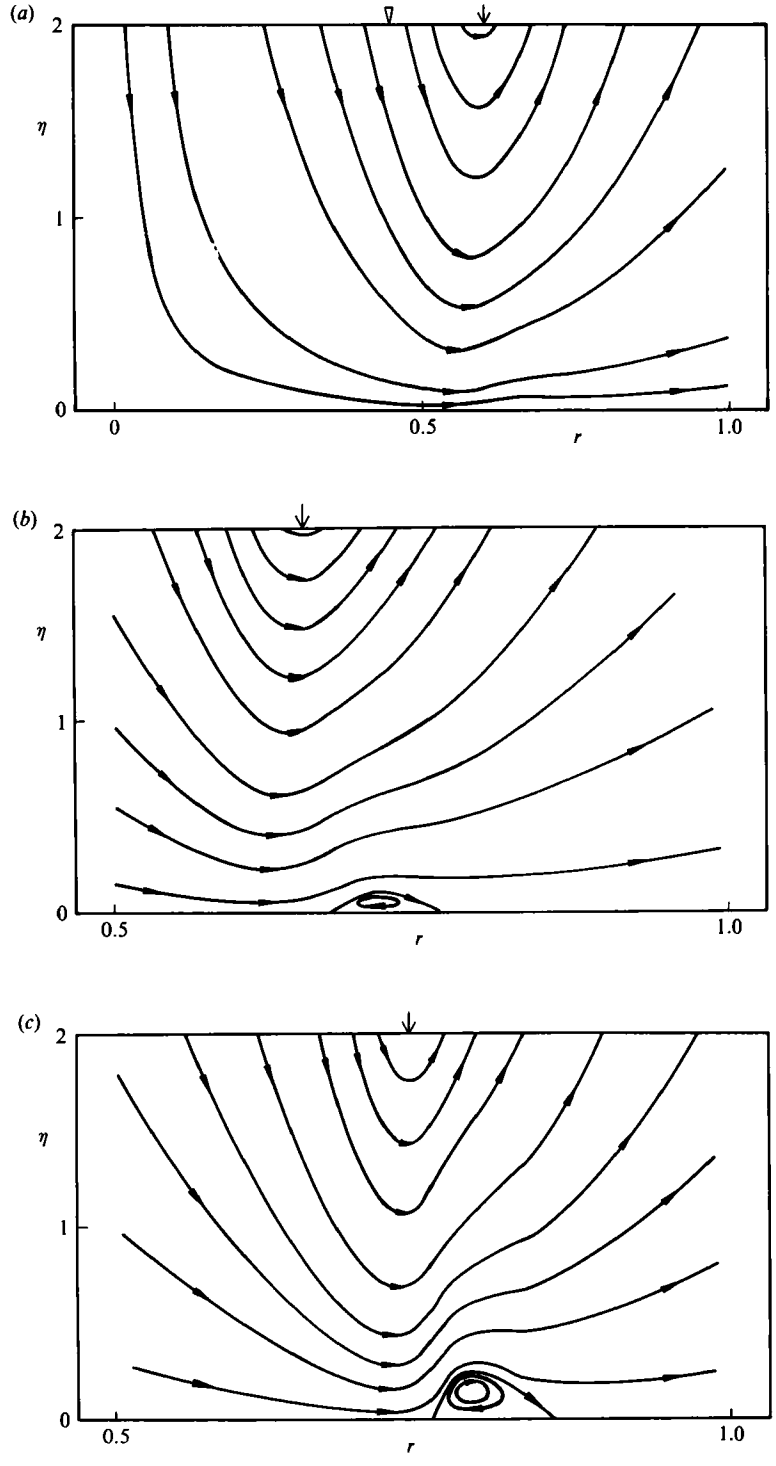

FIGURE 19(a–c). For caption see facing page.

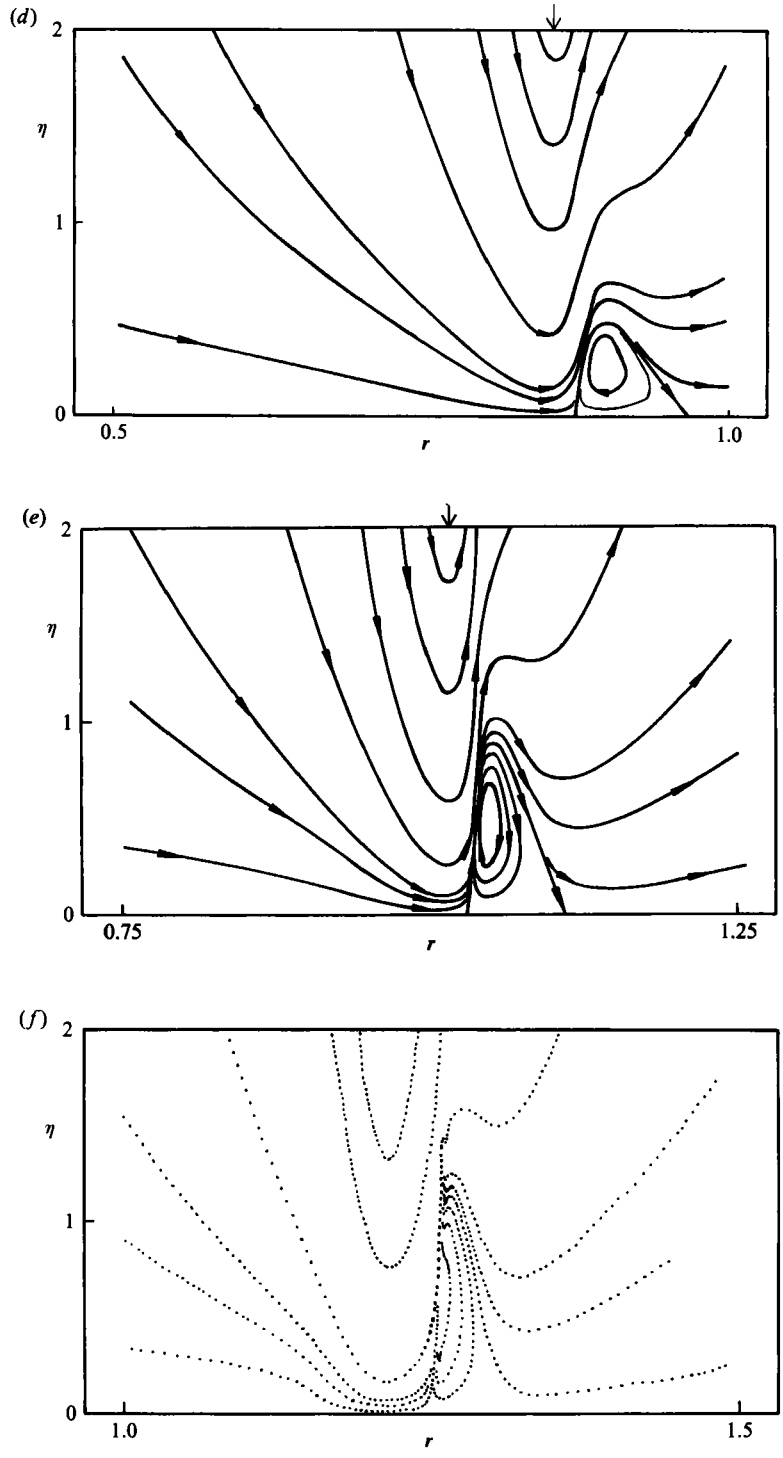

FIGURE 19. Instantaneous streamlines in the boundary layer at various times. (*a*) $t = 1.4$. (*b*) $t = 1.5$. (*c*) $t = 1.6$. (*d*) $t = 1.7$. (*e*) $t = 1.8$. (*f*) $t = 1.9$.

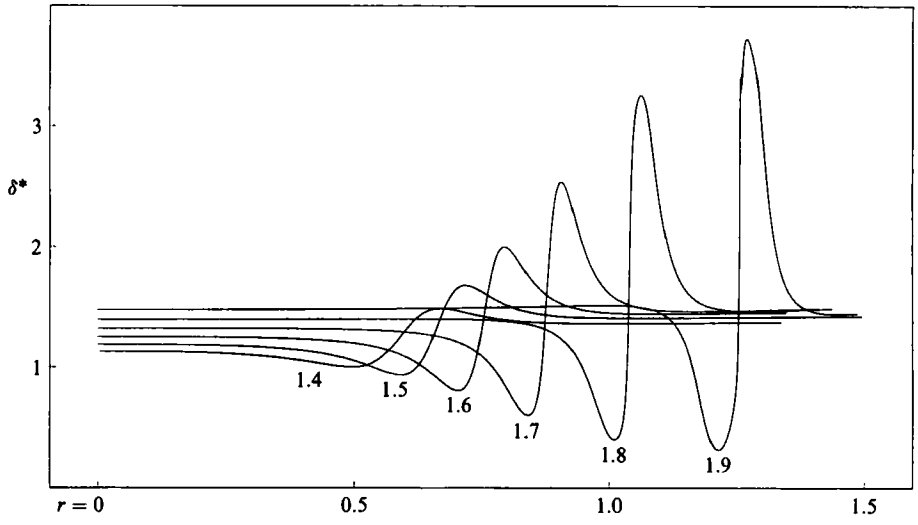

FIGURE 20. Temporal development of the displacement thickness; the labels correspond to dimensionless time.

of the vortex core while the vertical arrow denotes the current location of the core; arrows on the streamlines denote the direction of flow. A slight lifting of the streamlines near $r = 0.7$ may be observed in figure 19(*a*) and near this location separation occurs at $t = 1.428$ in the form of a recirculating secondary eddy which is attached to the wall. The separated region may be observed in figure 19(*b*) at $t = 1.5$. As time increases the separated eddy develops rapidly, growing in a direction normal to the wall, as illustrated in figures 19(*c*) to 19(*e*). Note that as the primary vortex core continues to move radially outward, it is sweeping the secondary eddy outward along the wall. The situation at $t = 1.8$ is depicted in figure 19(*e*) where it may be seen that in addition to the rapid normal growth rate, the eddy is being progressively compressed in the streamwise direction. The relative closeness of the streamlines on the left-hand side of the eddy are an indication of the intense variations that are developing there. It may also be observed that the streamlines which approach the secondary eddy develop an increasing distension with time, as they are forced to climb over the expanding region of recirculating flow. At this stage, significant upwelling is occurring on the left-hand side of the secondary eddy.

To illustrate the boundary-layer growth, a displacement thickness may be defined according to

$$\delta^* = \int_0^\infty (1-U)\,\mathrm{d}y. \tag{55}$$

The temporal development of δ^* is depicted in figure 20. It may be observed that the boundary layer is growing dramatically near the secondary eddy and the displacement thickness on the left-hand side is approaching the vertical. It is of interest to note that the boundary-layer growth is rather more dramatic than in the two-dimensional case considered by Walker (1978); as the ring moves toward the wall, vortex stretching leads to an increase in the local vorticity level and the separation process in the boundary layer intensifies.

Despite the relatively small mesh sizes that were employed in the present study, it becomes progressively more difficult to extend the numerical integrations signifi-

cantly past the stage depicted in figure 19(*e*). Thus the alternative forward–backward differencing method described by Doligalski & Walker (1984) was also used in the present study. This scheme ultimately failed to converge as well at later times; streamline patterns in the terminal stages are depicted in figure 19(*f*). At the stage indicated in figure 19(*f*), the numerical solutions are of questionable accuracy, particularly on the left-hand side of the secondary eddy, and the results are suggestive of the early stages of the development of a singularity in the boundary-layer solution at finite time. Such a singularity is known to occur in two-dimensional unsteady boundary-layer flows (Van Dommelen & Shen 1980; see also Ece, Walker & Doligalski 1984) and a similar behaviour is expected in this case as well. In effect, the singularity develops because of the attempt in the present calculation method to impose the outer inviscid velocity distribution (due to the primary vortex) on the boundary-layer solution for an indefinite period of time. It is clear from figures 19(*f*) and 20 that the boundary-layer flow is rapidly evolving toward a viscous–inviscid interaction with the outer flow. Therefore at the stage indicated in figure 19(*f*), it is apparently necessary to reformulate the problem and adopt a computational approach which permits a strong interaction between the boundary layer and the outer flow. To date the development of such an approach (other than full Navier–Stokes calculations at relatively low Reynolds numbers) has not been possible. However, the calculated results up to the stage of figure 19(*f*) are highly suggestive of a boundary-layer eruption and an ejection of the secondary eddy. This expectation has been verified by the experimental results discussed in §5. A detailed sequence of the process is illustrated in figure 21 which is a dual view visualization (using a surface dye sheet) of the response of the surface fluid to a vortex ring impact. Since the primary vortex ring was not visualized, the time origin in figure 21 was initiated arbitrarily (figure 21*a*) with the appearance of a noticeable clear region within the dye sheet. The development of this clear region is the result of lateral spreading of the dyed surface fluid away from the axis of the impinging vortex. Note that the progressive development of a clear region is quite obvious in the top views of figures 21 (*a*)–21 (*d*), while the corresponding side-views reveal no evidence of such development. This is because the side-views actually were taken at a slight downward angle (2° to 3°) to the plane of the plate and the dye sheet on the surface behind the point of interaction tends to obscure those motions which do not project significantly above the surface layer. Thus, figures 21 (*a*)–21 (*d*) indicate that, although the surface fluid is transported laterally away from the axis of the impinging vortex ring, there is little movement of the fluid away from the surface. This is consistent with the predicted behaviour in figure 20, which indicates slow initial growth of the displacement thickness. In figure 21 (*e*), the first evidence of a boundary-layer eruption (labelled E in the figure) is detected visually. This eruption approximately corresponds to the onset of substantial boundary-layer growth, indicated at $t \approx 1.9$ in figure 20. Note that the initial eruption grows quite rapidly and culminates in the ejection of a secondary vortex, the visual manifestation of which is indicated by an S in figures 21 (*g*) and 21 (*h*). The secondary vortex then interacts with the primary vortex and migrates toward the centre axis of the impinging vortex. This sequence shows clearly the initially slow boundary-layer development followed by the rapid eruption–ejection behaviour suggested by the numerical results.

Lastly, it is of interest to make a comparison between the separation time predicted by the theory and the experimental observations. The time to formation of the secondary vortex ring was measured relative to the instant when the primary vortex ring was one principal diameter away from the surface. The first occurrence of

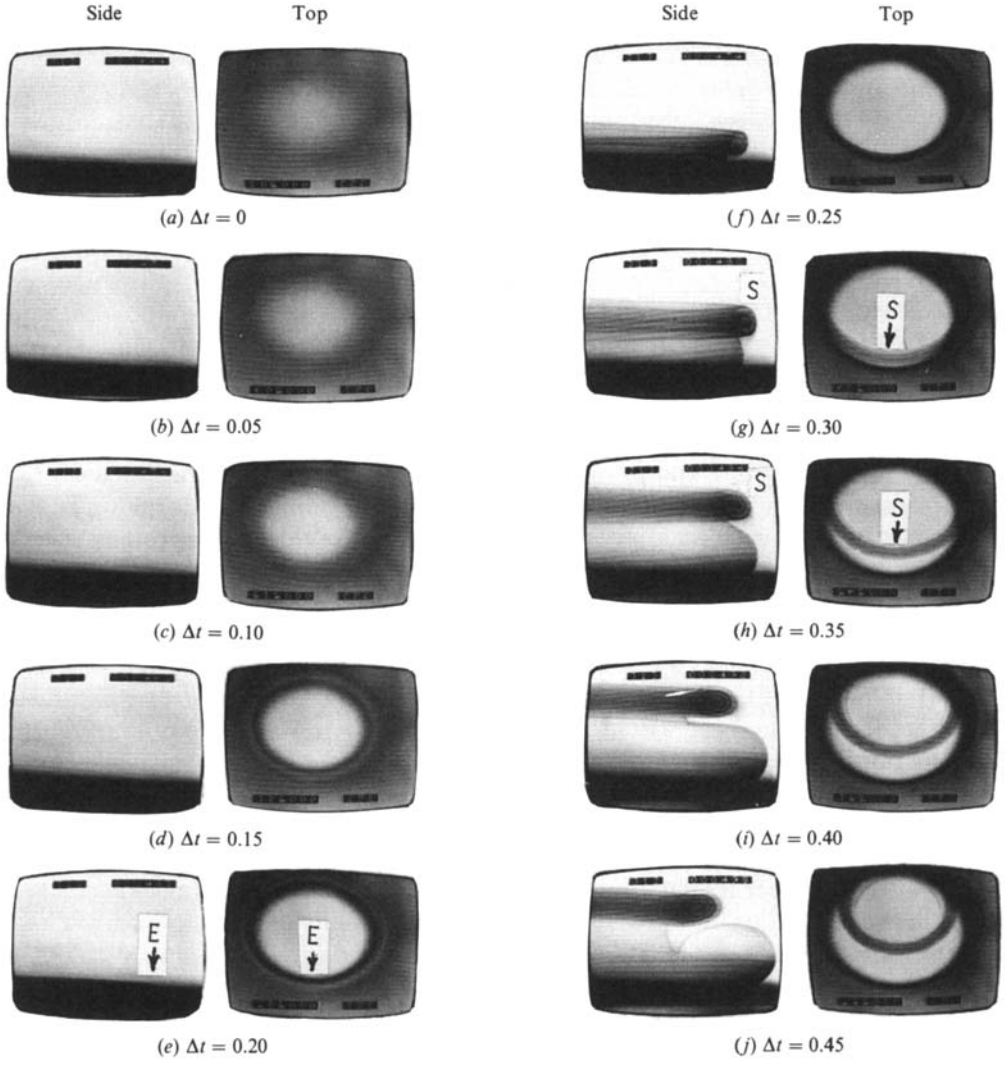

FIGURE 21. Dual side-top view visualization of response of surface dye sheet to vortex ring impact. E, initial ejection of fluid from surface. S, secondary vortex formed from roll-up of ejected surface fluid. Picture time units are seconds.

boundary-layer separation, in the form of a small attached eddy on the wall, is extremely difficult to detect experimentally and this was not feasible with the present apparatus. (Note that the trajectory of the primary ring and the boundary-layer flow were not visualized simultaneously.) It was however possible to measure a time t_s^* corresponding to the first indication of the presence of a secondary vortex. This was designated as the time when the dyed primary vortex was first deformed such that a noticeable concavity appeared in its outer surface. This type of measurement is somewhat sensitive to the subjective interpretation of the observer. As an example of the degree of primary vortex deformation that was required to indicate conclusive evidence of the presence of the secondary vortex, the measured formation time t_s^* for the sequence shown in figure 9 was determined to occur between the second and third

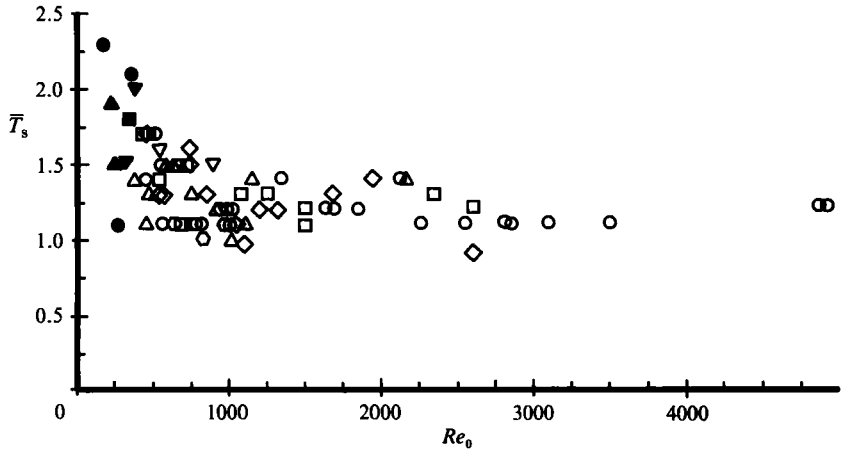

FIGURE 22. Dimensionless time of observation of the secondary vortex, $T_s = t_s V_0 = /D_0$ *vs.* Reynolds number Re_0. ▽, $D_M = 0.95$ cm; △, $D_M = 1.4$ cm; ◇, $D_M = 1.9$ cm; □, $D_M = 2.2$ cm; ○, $D_M = 2.5$ cm; ⬡, $D_M = 3.2$ cm. Solid symbols represent very weak vortices and indicate data based on very subjective observations

photographs in the first row. The normalized time to secondary vortex formation was defined as

$$\overline{T}_s = \frac{\bar{t}_s V_0}{D_0}, \tag{56}$$

where V_0 and D_0 are the initial velocity and diameter of the primary vortex ring. A plot of experimentally determined $\overline{T}_s$ versus Re_0 (the initial Reynolds number defined in (33)), is shown in figure 22 for 72 separate cases. It may be observed that $\overline{T}_s$ appears to change very slightly, if at all, with Re_0. At the lower Reynolds numbers, there is an apparently larger variation in $\overline{T}_s$, which is due to both the uncertainty in the measurements and the degree of subjectivity in establishing the first appearance of the secondary vortex. A lower initial Reynolds number is indicative of a weaker primary vortex and thus a correspondingly weaker secondary vortex; a weaker secondary vortex results in a smaller deformation in the primary vortex and makes the determination of $\overline{T}_s$ more uncertain. To indicate the high degree of uncertainty of some of the measurements at lower Reynolds numbers the corresponding data symbols have been filled in on figure 22. The average value of $\overline{T}_s$ measurements is 1.3 with a standard deviation of 0.3.

The numerical calculation was started at frame 513 of the sequence depicted in figure 3, for which $D_0 = 1.18$ cm, $Y_0 = 1.18$ cm, $L = 1.32$ cm, $V_0 = 6.48$ cm/s and $Re_0 = 727$; the value estimated for circulation by the method discussed in §6 was $\Gamma = 17.5$ cm^2/s. The dimensionless time t_s computed in the numerical solution until separation first occurs was $t_s = 1.428$ and a dimensionless time T_s may be defined according to

$$T_s = \frac{V_0}{D_0}\frac{L^2}{\Gamma} t_s. \tag{57}$$

The theoretical computed value from (57) is $T_s = 0.78$. This value is generally consistent with a value of the parameter $\overline{T}_s = 1.25$ obtained for the same set vortex parameters as well as the average value of $\overline{T}_s = 1.3$ obtained as an average of all

experiments. The parameter T_s measures the time to onset of separation, while $\overline{T}_s$ is a measure of the time required for the separation to have a noticeable effect on the primary vortex. Thus it is expected that T_s should have a lower value than $\overline{T}_s$, since there must be a lag between the point of initial eddy formation and the point when the eddy has grown to sufficient strength and size to produce an observable effect on the primary ring. An estimate of the order of magnitude of this lag may be obtained from figure 20; the Δt corresponding to the time from separation ($t = 1.428$) until the displacement thickness has achieved relatively large values at $t = 1.9$ is $\Delta T = 0.472$. This interval, in terms of the same measure as $\overline{T}_s$, is $\Delta T = \Delta t L^2 V_0/(D_0 \Gamma) = 0.26$. Consequently with $T_s + \Delta T = 1.04$, it is apparent from figure 22 that the comparison between the experiments and the theoretical predictions is encouraging.

9. Conclusions

The motion of a circular laminar vortex ring which moves on a trajectory normal and toward a plane wall has been investigated in this study. The experimental and theoretical results show that as the ring approaches the wall within a distance comparable to its diameter, an important unsteady boundary-layer effect begins to develop and strengthen on the wall. Boundary-layer separation occurs in the form of a secondary eddy attached to the wall in a ring which is located at radial distances greater than the radius of the primary ring. As the primary ring continues to move toward the wall, its rate of approach slows and its radius continues to increase; at the same time, the separated secondary ring in the boundary layer develops rapidly, and explosive boundary-layer growth begins to occur at radial locations near the inside edge of the secondary eddy. A viscous–inviscid interaction soon occurs between the outer flow and the thickening boundary layer; in this interaction the secondary eddy detaches from the wall and is ejected from the boundary layer as a secondary vortex ring. The secondary ring then interacts with the primary ring to arrest its radially outward motion and cause the primary ring to rebound from the wall. In most cases, the primary ring is then observed to induce a tertiary ring in the boundary layer, and at the higher Reynolds numbers a second eruption of the boundary-layer flow. The net effect is to completely arrest the motion of the primary vortex toward the wall and to either stop or reverse the radial expansion of the primary ring.

The experiments were carried out with stable laminar primary vortex rings. After the secondary ring was ejected from the boundary layer, wavelike instabilities were observed to occur and the flow field began to degenerate progressively into smaller scale three-dimensional motions. This process is complicated and Reynolds-number dependent; it has been documented in detail elsewhere (Cerra & Smith 1983). However the end result is an apparently chaotic flow which appears to be turbulent; a similar phenomenon has recently been observed by Didden & Ho (1985) who have investigated the boundary-layer response to a forced air jet impinging normally on a plane wall. The periodic forcing of the air jet results in a series of vortex rings which are convected toward the wall on the perimeter of the jet. The vortices were observed to induce secondary vortices in the unsteady boundary layer on the wall; after several eruptions were observed, the boundary-layer flow, in a direction away from the point of impingement, soon develops into an apparently chaotic and turbulent state.

The present study is fundamental, but of interest in the sense that it clearly shows how the motion of one vortex can lead to the production of other vortices near a wall. It also clearly demonstrates a basic physical effect wherein initial vorticity in a flow

can lead to the introduction of new vorticity from the wall region via an intermittent and abrupt eruption of the viscous flow near the wall. The similarity to some of the characteristics of bursting in a turbulent boundary layer should be noted (Walker, Scharnhorst & Weigand 1986). However it should also be pointed out that the vortex configurations in a turbulent boundary layer are believed to be more complicated than the ring vortices considered here; such vortices are probably of the hairpin type (Acarlar & Smith 1984, 1987*a*, *b*). The nature of the unsteady flow induced at a wall by moving hairpins is a complex problem which must await further research.

The authors are grateful for support of this work by the Air Force Office of Scientific Research under Contract Numbers F49620-78-C-0071 and F49620-81-K-0033.

REFERENCES

ACARLAR, M. S. & SMITH, C. R. 1984 An experimental study of hairpin-type vortices as a potential flow structure of turbulent boundary layers. *Report FM-5*, Department of Mechanical Engineering and Mechanics, Lehigh University, Bethlehem, Pa.

ACARLAR, M. S. & SMITH, C. R. 1987*a* A study of hairpin vortices in a laminar boundary layer. Part 1. Hairpin vortices generated by a hemisphere protruberance. *J. Fluid Mech.* **175**, 1–42.

ACARLAR, M. S. & SMITH, C. R. 1987*b* A study of hairpin vortices in a laminar boundary layer. Part 2. Hairpin vortices generated by fluid injection. *J. Fluid Mech.* **175**, 43–83.

BLASIUS, H. 1908 Grenzschichten in Flussigkeiten mit kleiner Reibung, *Z. angew. Math. Phys.* **56**, 1–37.

BLISS, D. B. 1970 The dynamics of curved rotational vortex lines. MS thesis, MIT.

BOLDES, U. & FERRERI, J. C. 1973 Behavior of vortex rings in the vicinity of a wall. *Phys. Fluids* **16**, 2005–2006.

BRASSEUR, J. G. & CHANG, I.-D. 1981 Combination of kinematics with flow visualization to compute total circulation, *AIAA J.* **19**, 878–884.

CERRA, A. W. & SMITH, C. R. 1983 Experimental observations of vortex ring interaction with the fluid adjacent to a surface. *Report FM-4*. Department of Mechanical Engineering and Mechanics, Lehigh University, Bethlehem, PA.

DENNIS, S. C. R. & WALKER, J. D. A. 1971 The initial flow past an impulsively started cylinder, *J. Engng Maths* **5**, 263–278.

DIDDEN, N. 1977 Untersuchung laminarer, instabiler Ringwirbel mittels Laser-Doppler-Anemometrie. *Mitt Nr.* 64, Göttingen: Max-Planck-Inst. Strömungsforschung.

DIDDEN, N. & HO, C.-M. 1985 Unsteady separation in a boundary layer produced by an impinging jet. *J. Fluid Mech.* **160**, 235–256.

DOLIGALSKI, T. L. 1980 The influence of vortex motion on wall boundary layers. PhD thesis, Lehigh University.

DOLIGALSKI, T. L., SMITH, C. R. & WALKER, J. D. A. 1980 A production mechanism for turbulent boundary layers. *Prog. Astr. Aero.* **72**, 47–72.

DOLIGALSKI, T. L. & WALKER, J. D. A. 1984 The boundary layer induced by a convected two-dimensional vortex. *J. Fluid Mech.* **139**, 1–28.

ECE, M. C., WALKER, J. D. A. & DOLIGALSKI, T. L. 1984 The boundary layer on an impulsively started rotating and translating cylinder. *Phys. Fluids* **27**, 1077–1089.

ERSOY, S. & WALKER, J. D. A. 1985*a* Viscous flow induced by counter-rotating vortices. *Phys. Fluids* **28**, 2687–2698.

ERSOY, S. & WALKER, J. D. A. 1985*b* The viscous flow induced near a wall by counter-rotating vortex pairs and vortex loops. *Report FM-8*, Department of Mechanical Engineering and Mechanics, Lehigh University, Bethlehem, PA.

FRAENKEL, L. E. 1972 Examples of steady vortex rings of small cross-section in an ideal fluid. *J. Fluid Mech.* **51**, 119–135.

HARVEY, J. K. & PERRY, F. J. 1971 Flowfield produced by trailing vortices in the vicinity of the ground. *AIAA J.* **9**, 1659–1660.

HELMHOLTZ, H. 1867 On integrals of the hydrodynamic equations which express vortex motion. *Phil. Mag.* **33**, 485–512.

HICKS, W. M. 1884 On the steady motion and the small vibrations of a hollow vortex. *Phil. Trans. R. Soc. Lond.* A **175**, 161–195.

JAHNKE, E. & EMDE, F. 1945 *Tables of Functions with Formulae and Curves*, 4th edn. Dover.

LAMB, H. 1932 *Hydrodynamics*, 6th edn. Cambridge University Press.

LEONARD, A. 1980 Vortex methods for flow stimulation. *J. Comput. Phys.* **37**, 289–335.

LEONARD, A. 1985 Three-dimensional vortex flows. *Ann. Rev. Fluid Mech.* **17**, 523–559.

MAGARVEY, R. H. & MACLATCHY, C. S. 1964 The formation and structure of vortex rings. Can. J. Phys. **42**, 678–689.

MAXWORTHY, T. 1977 Some experimental studies of vortex rings. *J. Fluid Mech.* **81**, 465–495.

MILNE-THOMSON, L. M. 1963 *Theoretical Hydrodynamics*, 4th edn. Macmillan.

NYCHAS, S. G., HERSHEY, H. C. & BRODKEY, R. S. 1973 A visual study of turbulent shear flow. *J. Fluid Mech.* **61**, 513–540.

PEACE, A. J. & RILEY, N. 1983 A viscous vortex pair in ground effect. *J. Fluid Mech.* **129**, 409–426.

RILEY, N. 1975 Unsteady laminar boundary layers. *SIAM Rev.* **17**, 274–297.

SAFFMAN, P. G. 1970 The velocity of viscous vortex rings. *Stud. Appl. Maths* **49**, 371–380.

SAFFMAN, P. G. 1975 On the formation of vortex rings. *Stud. Appl. Maths* **54**, 261–268.

SAFFMAN, P. G. & BAKER, G. R. 1979 Vortex Interactions. *Ann. Rev. Fluid Mech.* **11**, 95–122.

SALLET, D. W. & WIDMAYER, R. S. 1974 An experimental investigation of laminar and turbulent vortex rings in air. *Z. Flugwiss* **22**, pp. 207–215.

SCHNEIDER, P. E. M. 1978*a* Morphologisch-phänomenologische Untersuchung der Umbildung von Ringwirbeln, die Körper anströmen, Göttingen: Max-Planck-Inst. Strömungsforchung.

SCHNEIDER, P. E. M. 1978*b* Werden, Bestehen, Instabilität, Regeneration, Vergehen eines Ringwirbels, Göttingen: Max-Planck-Inst. Strömungsforschung.

SEARS, W. R. & TELIONIS, D. P. 1975 Boundary-layer separation in unsteady flow. *SIAM J. Appl. Maths* **28**, 215–235.

SMITH, C. R. & METZLER, S. P. 1983 The characteristics of low-speed streaks in the near-wall region of a turbulent boundary layer. *J. Fluid Mech.* **129**, 27–54.

SULLIVAN, J. P., WIDNALL, S. E. & EZEKIEL, S. 1973 Study of vortex rings using a laser doppler velocimeter. *AIAA J.* **11**, 1384–1389.

TUNG, C. & TING, L. 1967 Motion and decay of a vortex ring. *Phys. Fluids* **10**, 901–910.

VAN DOMMELEN, L. L. & SHEN, S. F. 1980 The spontaneous generation of the singularity in a separating laminar boundary layer. *J. Comp. Phys.* **38**, 125–140.

WALKER, J. D. A. 1978 The boundary layer due to a rectilinear vortex. *Proc. R. Soc. Lond.* A **359**, 167–188.

WALKER, J. D. A., SCHARNHORST, R. K. & WEIGAND, G. G. 1986 Wall layer models for the calculation of velocity and heat transfer in turbulent boundary layers. *AIAA paper* 86-0213.

WIDNALL, S. E., BLISS, D. B., ZALAY, A. 1971 Theoretical and experimental study of the stability of a vortex pair. In *Aircraft Wake Turbulence and its Detection* (ed. G. Goldberg & R. Rogers), pp. 305–338. Oslo.

WIDNALL, S. E. & SULLIVAN, J. P. 1973 On the stability of vortex rings. *Proc. R. Soc. Lond.* A **332**, 335–353.

YAMADA, H. & MATSUI, T. 1980 Visualization of vortex interaction using smoke-wire technique. *International Symposium of Flow Visualization, Bochum, Germany, Ruhr-Universität Bochum, Inst. für Thermo und Fluiddynamik.*